SAPIENZA
UNIVERSITÀ DI ROMA

Analysis, design and optimization of broadband microwave filters for high-power applications

Fabrizio DE PAOLIS

Università "La Sapienza" di Roma
Facoltà di Ingegneria

Dottorato di Ricerca in Elettromagnetismo
XXV Ciclo: novembre 2009 - ottobre 2012

Coordinatore del Corso:

Prof. Paolo LAMPARIELLO

Docente guida:

Prof. Fabrizio FREZZA

To my wife.

Contents

Chapter 1. Introduction

Modern telecommunication satellites are becoming progressively more complex as a consequence of the growing number of carriers and increasing Equivalent Isotropic Radiated Power (EIRP), together with the trend of integrating multiple missions, different frequency bands and multi-beam antennas on-board of a single satellite platform. Typical features are the use of two or more Traveling Wave Tube Amplifiers (TWTA) combined at the output to generate high-power and flexible transponders [1], as well as the implementation of several large payloads with complex repeater and antenna layouts [2]. In a conventional bent-pipe architecture, the number of passive RF units quickly grows with the increasing requirement of satellite capacity, up to the point where severe limitations are encountered at platform level for practical reasons (mass, size and/or power). Furthermore, the number of interconnections required between different RF equipment and subsystems considerably increases in complexity, leading to major challenges in the payload integration and test.

Today, communication satellites operate in multicarrier mode, with powers of several hundreds of Watts per channel. Future commercial Fixed Satellite Systems (FSS) and Broadcast (BSS/DBS), will demand both higher power per beam and larger payloads offering hybrid coverage (global/regional and spot beams). Satellite operators are currently concentrating on Ku and Ka-band geostationary satellites, with an increasing interest for the Reverse Bands (21.4 – 22.0 GHz in Europe, 17.3 – 17.8 GHz in the Americas). In parallel, it is foreseen that payloads with low-number of broadband transponders will challenge the narrowband channelization approach currently used. Such trend will follow the development of power amplifiers technologies [3].

Fig. 1-1 depicts the simplified block diagram of a generic bent-pipe telecommunication payload. It presents a large number of channel filters, in order to efficiently handle a complex and congested frequency spectrum. The output passive RF chain after the Output Multiplexer (OMUX) is subjected to the high power signals coming from the TWTAs. Assuming a 15 channel OMUX with 300 Watt per channel, the maximum instantaneous power at the output section is 67.5 kW, since the peak power increases with the square of the number of carriers ($P_{peak} = N^2 \cdot P$). The block diagram of Fig. 1-1 also show high power transmitters (e.g., over 100 Watts) at many frequencies used in proximity of high sensitivity receivers (e.g., below -120 dBm). In order to minimize size occupation, hardware is compactly packed in the satellite and/or antenna tower through diplexing functions.

The trend of spacecraft design with large bandwidths, high component integration and increasing power handling capability, leads to both high electric field densities inside microwave devices and increasing risks of signal cross-talking. Due to the space environment and high electric fields, generated free electrons may cause discharge phenomena of different nature inside on-board microwave devices; moreover, the use of very high power transmitters in proximity of ultra-sensitive receivers may cause unacceptable non-linear behaviour. As a consequence, equipment failure and RF link degradation are major high-power issues to be faced by RF engineers. Depending on the application, two kinds of phenomena can occur within a high-power RF passive device [4]:

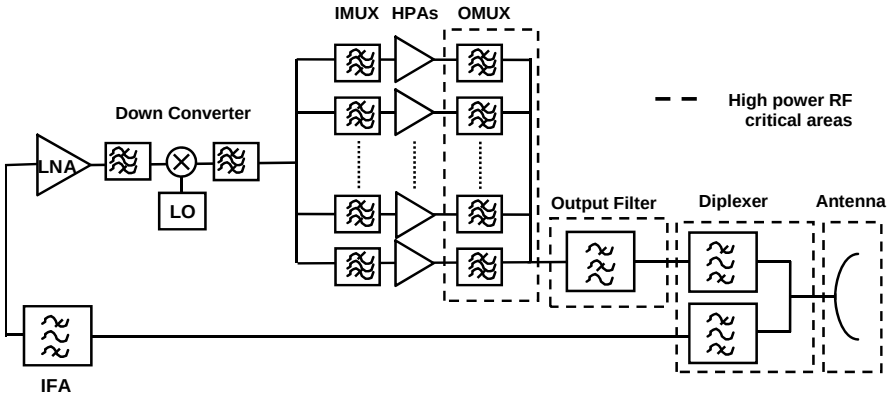

Fig. 1-1: Simplified block diagram of a conventional bent-pipe communication payload.

- **Multipactor breakdown** - At very low-pressure range or vacuum, free electrons are strongly accelerated by the harmonic electric field, since there is no gas o other material stopping their motion. Under certain conditions, electrons continuously hit the wall of the microwave cavities, leading to an avalanche-like increase of electrons by secondary emission. Multipactor can occur in both single-carrier and multi-carrier systems and is highly harmful for the hardware performance and integrity.

- **Passive Intermodulation (PIM) effect** - This intrinsic multi-carrier phenomenon can be viewed as a generalized intermodulation effect, where interference between carriers results in a malfunctioning of the overall satellite communications system. Its origin is in the existence of a non-linear behaviour in the passive components integrated within final stages of communication payloads. If several carriers are present in the system, intermodulation products are excited. PIM signals originated in the transmission band of the satellite can fall in the receive band. Although the excited signals are typically very low power, the received signals are also at a similarly low level, leading to a risk of interference.

Furthermore, other RF breakdown phenomena must be also assessed for many space equipment, such as corona and dielectric breakdown. These are at least as harmful as multipactor and PIM, but are somewhat less general, more application-specific and are outside the scope of this work.

Multipactor and PIM – more generically classified as *non-linear RF phenomena* in passive devices – have in common the negative effects on the availability of the communications link. Multipactor breakdown is typically observed as an increase of reflection losses, non-linearity and noise levels, ultimately leading to destructive, non-recoverable effects on the hardware. The generation of PIM products cause receiver desensitization, which is extremely difficult to control due to the highly workmanship dependency of the phenomenon and its persistence at both component and system level. When multipactor and/or PIM are not adequately addressed, the system performance degradation and even the total loss of one or more transponders become a concrete risk. It shall be mentioned however that multipactor – at least in the single-carrier case – is a relatively well understood and consistent RF failure mode. There exist a large quantity of reference material, together with established analysis and test techniques. PIM is instead a considerably more complex phenomenon and cannot be predicted accurately due to its erratic nature. Up to date, PIM remains an issue to be tackled mainly at manufacturing, assembly and test levels.

The standard ECSS-E-20-01A [5] of the European Cooperation for Space Standardization (ECSS) defines the guidelines and requirements related to multipactor for designing and testing

high power RF space hardware. The standard covers the conservative cases of single non-modulated CW carrier and multiple non-modulated CW carriers combined. For what concerns multicarrier operation, only recommendations are provided due to the lack of experimental data for validation. Two cases are considered in the ECSS standard:

1. Design based on the worst-case $N^2 \cdot P$ peak power experienced by the signal and test based on a single carrier of equivalent peak power, with the addition of a defined margin.
2. Design based on the so called P_{20} rule (electrons shall cross the gap at least 20 times in order for the breakdown to be detectable).

However the current standard has two separate limitations. First, it can lead to over-design and over-test, when using the absolute peak power recommendation. Second, it can lead to unconsolidated margins if based on the P_{20}/T_{20} approach, due to the uncertainty in defining a P_{20}. Both limitations can have severe consequences on the design and test requirements for space RF hardware.

1.1 Impacts of modulation scheme and filters on waveform envelope

Most of the signals used in modern communication systems are digitally modulated. As a consequence of the scarcity of spectrum available, the signal engineers are pushing for modulation schemes which are more spectrally efficient (i.e., more bits per Hertz of spectrum). This leads to more complicated modulation scenarios which are often associated with signals presenting large peak to average ratios. The Complementary Cumulative Distribution Function (CCDF) curves show that, despite of a mild average power, an instantaneous signal power can reach very high levels, sometimes up to 10 dB above the average transmitted power. The peak amplitude in the CCDF curve is normally referred as the Peak to Average Power Ratio (PAPR) of the signal. This parameter is important for considerations related to multipactor. For a signal *s(t)* of average power P_{rms} and peak power P_{peak}, PAPR is defined as (values for commonly used modulation schemes are reported in Table 1):

$$PAPR = 10\log\frac{\max\left\{|s(t)|^2\right\}}{\int_{-\infty}^{+\infty}|s(t)|^2\,dt} = 10\log\frac{P_{peak}}{P_{rms}} \tag{1.1}$$

TABLE I
PAPR FOR DIFFERENT MODULATED SIGNALS

Signal Type	PAPR (Typical)
CW	3 dB
Pulsed CW	$20\log(2T/T_{on})$
QPSK (α=0.2)	≈5.6 dB
16APSK (α=0.2)	≈6.3 dB
32APSK (α=0.2)	≈6.7 dB
IS-95 CDMA (Single Carrier)	≈10 dB
WCDMA/UMTS (Multicarrier)	≈12.2 dB

Fig. 1-2: Gibbs effect on a filtered square wave signal [6].

In addition to the intrinsically non-constant amplitude distribution of digitally modulated signals, the Gibbs phenomenon (Fig. 1-2) may introduce additional peaks in filtered signals. In fact, depending on the filter frequency response and on the nature of the modulated signals, the phenomenon may be more or less problematic.

In [6] it has been shown that for very short duration of pulses (with no or limited electron cloud history), the onset of Multipactor requires significantly more energy. In order to avoid relying on empirical prediction models such as P_{20}/T_{20}, or on the worst case approach (i.e. absolute peak power in a signal), it is possible to test hardware in conditions close to operational condition, i.e. "test as fly". This allows including peculiarities related to signal modulations (e.g. repetition cycle of the peaks and associated electron cloud growth, or phase rotation of the modulated carrier). It has been understood that the effect of the filter in the communication chain may not be ignored when determining peak signal strength, as the filter can increase the peak to average signal ratio. If this is the case, test margins with respect to the peak signal strength at the output need to be defined, rather than with respect to the signal strength at the input. The test with realistic modulated signals allows determining with a solid basis the hardware limits for the operational conditions, including the real margin embedded in the design. The limitation of this approach consists in identifying a representative test condition over a multitude of signals potentially applicable. There could be cases (e.g. navigation payloads) where those signals are precisely known, however in most of telecommunication satellites a large number of signal types exists, which sometimes cannot even be defined a priori. Further investigation is therefore required on the viability of this approach.

1.2 17/24 GHz Reverse Broadcast Satellite Service (BSS)

Another interesting case-study from the multipactor viewpoint is the new U.S. 17/24-GHz broadcast satellite service (Reverse BSS) frequency range. In most of the proposed satellite architectures [7], a common element to achieve sufficient power flux density on ground is the anticipated use of single OMUX assemblies carrying up 8 to 16 narrow bandwidth channels, all at very high power. Ka-Band Satellite payloads with a maximum of 250 W per channel are today state of the art. This trend is pushed forward by the Reverse BSS desire for higher RF power and narrower channel bandwidths. In this context the peak power generated at the output section from the OMUX to the antenna (manifold, output filtering and feed elements) increases drastically. In parallel, the overall OMUX thermal management represents another design issue that will need to be separately addressed. Because of these technical challenges, it is expected that the OMUX and its output section will be the critical payload element for future Reverse BSS applications. In [8] multicarrier analyses were performed for the payload output section in accordance to the ECSS recommendations, considering realistic scenarios envisaged by satellite operators. Typical RF power levels are in the range of 250 to 500 W per channel. Examples of 8 channel OMUX were presented with different power levels for each case. In all cases studied, ECSS standard verification routes fail to provide sufficient analysis margin, while qualification or acceptance testing would

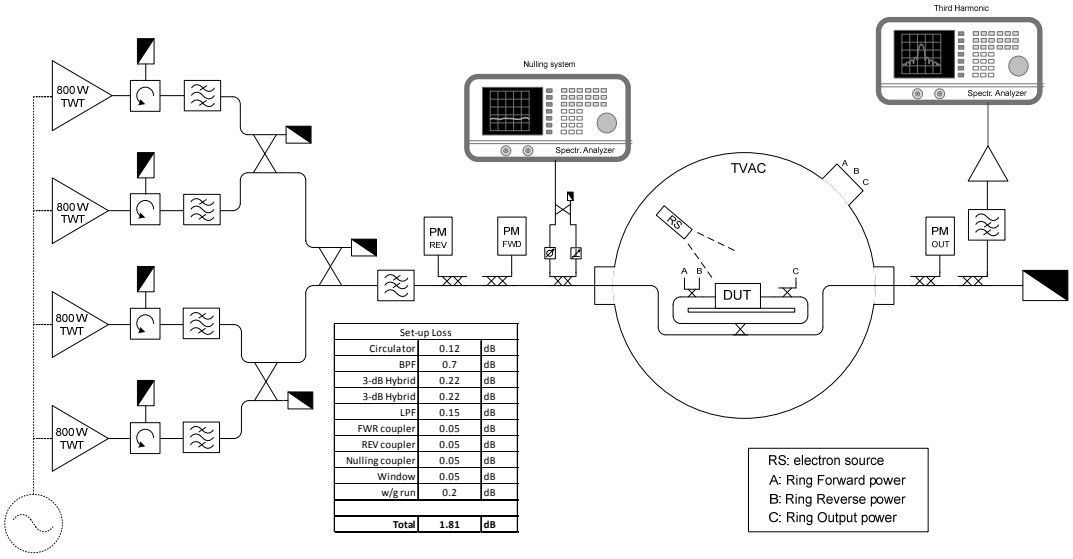

Fig. 1-3: 17 GHz BSS high power set-up schematic, including set-up insertion loss budget [8]

imply complex and costly RF test facilities. Fig. 1-3 shows the schematic of a high power test set-up proposed in [8], allowing both average power and multipactor testing of a DUT in a realistic Reverse BSS scenario. Although the proposed test facility is flexible and rather simple in concept, it would easily exceed the 1 M€ cost figure and still require a certain customization depending on the specific test conditions.

1.3 Motivations

Over the past years, there have been significant advances in the area of high power passive RF devices. Nevertheless, power handling (multipactor and PIM) continues to be a critical design aspect in particular for filters. This is due the complexity of the phenomena involved and their dependency on electromagnetic field strength, materials, geometry and operating conditions of the system. State-of-the-art high-power testing capabilities are essential when producing optimal space borne RF equipment. The discussion areas above demonstrated however that high-power testing can become extremely complex and costly, and hence is normally adopted as an ultimate resource when cannot be avoided. Therefore, it is imperative to perform high-power risk analysis as a part of design process. The main goals of previous research activities were to obtain a good understanding and to develop means of predictions for the simplest cases. Current trends are towards the creation and validation of powerful analysis tools capable to accurately characterize complex waveguide equipment like filters or multiplexers under high power operation. As performance and costs are the main drivers in satellite applications, realistic margins should be chosen to avoid on one hand hardware failure, on the other hand excess cost through component over specification.

The analysis and design of high power RF hardware for space applications represent therefore areas of particular interest in today's electromagnetics research. The objective here is to cover two relevant topics: 1) accurate *analytical* tools to assist in the prediction of RF breakdown levels in filters; 2) development areas for output filters (such as bandpass filters/diplexers and harmonic filters), with emphasis on novel design concepts and methods to obtain *optimal* filter performance. Both areas have found limited attention in the technical literature when *broadband filters* are

considered. Furthermore, broadband filters and multiplexers play a key role in current and next generation high-power satellite systems [9].

1.4 References

[1] C. Ernst, P. Angeletti and F. De Paolis, "Needs for Bandwidth Reconfigurable Filter Network for Space Applications," ESA Flexible Payload Workshop, Noordwijk, The Netherlands, April 2012.

[2] R. Singh and E. Hunsaker, "Systems Methodology for PIM Mitigation of Communications Satellites structures," 4th International Workshop on Multipactor, Corona and Passive Intermodulation in Space RF Hardware, 8-11 September 2003, Noordwijk, The Netherlands.

[3] A. E. Atia, "Wideband communication satellite payload architecture," Microwave Symposium Digest (MTT), 2011 IEEE MTT-S International, June 2011, pp. 1 – 4.

[4] W.-C. Tang and C. M. Kudsia, "Multipactor breakdown and passive intermodulation in microwave equipment for satellite applications," Military Communications Conference, MILCOM '90, pp. 181-187, vol.1, 30 September – 3 October 1990.

[5] "Multipaction design and test," European Space Agency, Noordwijk, The Netherlands, ECSS-E-20-01A, May 5, 2003.

[6] N. Le Gallou, C. M. Espanya, S. Matinfair, C. Ernst and F. De Paolis, "Multipactor Threshold and Margins Using Realistic Modulated Signals", International Workshop on Multipactor, Corona and Passive Intermodulation in Space RF Hardware, Valencia, Spain, September 2011.

[7] M. R. Björkman, "Overview of the U.S. 17/24-GHz Broadcast Satellite Service," 27th IET and AIAA ICSSC, Edinburg, UK, 1-4 June 2009.

[8] F. De Paolis and D. Lemus, "Multipactor Assessment of the new U.S. 17/24 GHz Broadcast Satellite Service," International Workshop on Multipactor, Corona and Passive Intermodulation in Space RF Hardware, Valencia, Spain, September 2011.

[9] H. Hu and K.-L. Wu, "Coping with spurious effects in full-wave electromagnetic design of a wide-band waveguide multiplexer," Microwave Symposium Digest (MTT), 2012 IEEE MTT-S International, June 2012, pp. 1 – 3.

Chapter 2. Voltage prediction in broadband filters

As transmit power levels of space communication systems increase, challenging high-power handling requirements flow down to lower level subsystem and component specification. The peak power handling capability has to be carefully analysed when designing high power hardware, in particular filters [1]. RF power handling requirements for multipactor [2], [3], and/or ionization breakdown [4], are defined. Breakdown estimation is then performed based on the predicted values of peak voltages (or electric fields) in the filter, with the target to avoid costly test campaign or design iterations. With today's 3D EM simulation tools, the filter designer can accurately predict voltages and electric fields. Depending on the complexity of the filter type, structure and topology, this process can be time consuming and requires detailed knowledge of the filter design dimensions. This represents a major limitation, in particular when filter performance has to be assessed in the early design stages of a complex RF system. It would be desirable to use instead methods which are fast, accurate and largely independent of the filter detailed design. In many cases, analytical prediction is sufficient to establish compliance to the power handling requirements: for example, the use of a circuit/electromagnetic hybrid approach could considerably improve the efficiency of analysis and design processes.

Consider a coupled prototype model [5] consisting of n capacitors of 1 F and n+1 normalized coupling elements $k_{i,i+1}$, which are calculated from the prototype elements g_i defined for a Chebyshev filter using the following:

$$k_{i,i+1}\Big|_{i=0,\ldots,n} = \frac{1}{\sqrt{g_i g_{i+1}}} \tag{2.1}$$

where n is the filter order. Source and load resistors are normalized to 1 Ω and a current source is set to 2 A. The prototype model is represented by the nodal admittance matrix Y [6], [7]:

$$Y = \begin{pmatrix} 1 & jk_{0,1} & 0 & 0 & 0 & 0 & 0 \\ jk_{0,1} & j\omega' & jk_{1,2} & 0 & 0 & 0 & 0 \\ \cdot & jk_{1,2} & j\omega' & jk_{2,3} & 0 & \cdot & \cdot \\ \cdot & \cdot & jk_{2,3} & \cdot & \cdot & \cdot & \cdot \\ \cdot & \cdot & \cdot & \cdot & \cdot & \cdot & \cdot \\ 0 & 0 & \cdot & \cdot & \cdot & j\omega' & jk_{n,n+1} \\ 0 & 0 & 0 & 0 & 0 & jk_{n,n+1} & 1 \end{pmatrix} = G + j\omega' + jM \tag{2.2}$$

where Y is composed of three sub-matrices:

1) a matrix jM of coupling factors (all elements purely imaginary);
2) a matrix G of source and load resistances (all elements are purely real);
3) a frequency variable diagonal matrix $j\omega'$ (all elements purely imaginary), where ω' is the angular frequency of the prototype filter. An element is zero when representing a non-resonating node.

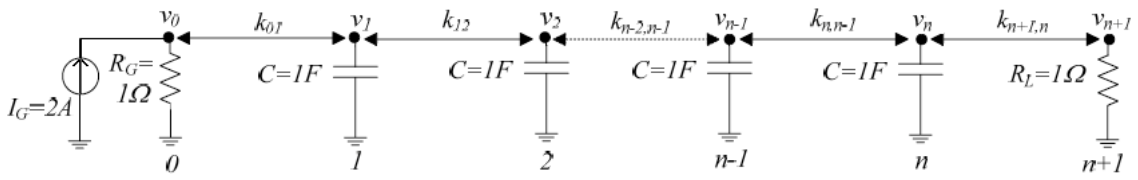

Fig. 2-1: Direct-coupled low-pass prototype filter.

Inverting matrix Y the following linear equation system can be solved for the peak voltages v_0, $v_1,\ldots, v_{n+1}$:

$$\begin{pmatrix} v_0 \\ v_1 \\ \cdot \\ \cdot \\ \cdot \\ v_n \\ v_{n+1} \end{pmatrix} = Y^{-1} \cdot \begin{pmatrix} 2 \\ 0 \\ \cdot \\ \cdot \\ \cdot \\ 0 \\ 0 \end{pmatrix} \tag{2.3}$$

The stored energy W_i in the i-th element of the filter prototype is given by:

$$W_i(f) = \frac{1}{4} C_i v_i^{\,2} = \frac{1}{4} v_i^{\,2} \tag{2.4}$$

The stored energy $W_{ph,i}$ in the i-th element of the filter physical realization is related to the stored energy W_i in the corresponding element of the prototype by the transformation [8]:

$$W_{ph,i}(f) = \frac{1}{2\pi} W_i(f) \frac{dT}{df} \tag{2.5}$$

where T is the frequency transformation linking the prototype to the filter physical realization.

Note the average input power of the prototype:

$$P_0 = \frac{v_0^{\,2}}{2} \tag{2.6}$$

2.1 Voltage prediction in bandpass filters

Bandpass filter field prediction based on circuit models was initially proposed in [9], however dispersion effects were not considered. Extensions of the theory of [9] were described in [10] and [11] where the concept of coupling matrix was used giving equations for the peak electric field as a function of the voltage in the filter prototype. In [12] electric field predictions of waveguide bandpass filters are related to the time-average stored energy in the lumped low-pass prototype network. The prediction of the peak electric fields is thus obtained directly from the circuit model. The formula published in [12] is limited to rectangular waveguide filters with rather narrow bandwidths. In the frame of this work, a more general approach using improved frequency transformations has been introduced. This results in analytical expressions to predict peak voltages and electric fields in rectangular, circular, and coaxial waveguide bandpass filters based on shunt

susceptive inverters, with better representation of dispersion effects in broadband applications. Furthermore, an analytical expression for evanescent-mode filters is proposed for the first time.

2.1.1 Bandpass filter frequency transformation

In order to take into account dispersion effects of waveguide bandpass filters, Levy describes a frequency transformation valid for inductive coupled cavity filters [13], expressed as a function of the guided wavelength:

$$T(f) = \omega' = \frac{\left(\frac{\lambda_g}{\lambda_{g0}}\right)\sin\left(\pi\frac{\lambda_{g0}}{\lambda_g}\right)}{\sin\theta_0'} \tag{2.7}$$

where

$$\sin\theta_0' = -\frac{\lambda_{g1}}{\lambda_{g0}}\sin\left(\pi\frac{\lambda_{g0}}{\lambda_{g1}}\right) = \frac{\lambda_{g2}}{\lambda_{g0}}\sin\left(\pi\frac{\lambda_{g0}}{\lambda_{g2}}\right) \tag{2.8}$$

It can be observed that in (2.8) the quantity λ_{g0} is unknown, while λ_{g1} and λ_{g2} are given and define the band-edges of the equal-ripple filter bandwidth. The quantity λ_{g0} represents the guided wavelength at the centre frequency of the filter under consideration. The non-linear equation (2.8) can be easily solved by numerical methods.

The frequency substitution T – valid for inductive coupling elements – enables mapping the low-pass prototype into the desired bandpass response by introducing (2.7) into (2.3). The derivative of T with respect to frequency is:

$$\frac{dT}{df} = \left(\frac{\lambda_g}{\lambda}\right)^2 \frac{\pi\cos\left(\pi\frac{\lambda_{g0}}{\lambda_g}\right) - \frac{\lambda_g}{\lambda_{g0}}\sin\left(\pi\frac{\lambda_{g0}}{\lambda_g}\right)}{f\sin\theta_0'} \tag{2.9}$$

Another important case to consider is that of evanescent-mode filters. These are usually realized from a rectangular waveguide below cut-off loaded by capacitive ridge sections. The evanescent sections act as coupling elements whereas the ridged sections act as half-wave resonators. Microwave filters of this type have a bandpass response and can be analysed with a lumped-constant approach, under certain conditions [14]. For wide bandwidths up to approximately 10%, the lumped-constant theory can be used, provided that an appropriate correction factor is introduced to account for the steeper slope parameters of the evanescent couplings compared to the lumped elements. Is then possible to use the frequency transformation:

$$T(f) = \omega' = \frac{f_0}{BW}\left(\frac{f}{f_0} - \frac{f_0}{f}\right) \tag{2.10}$$

where f_0 and BW are the filter center frequency and bandwidth respectively.

The derivative of T with respect to frequency is:

$$\frac{dT}{df} = \frac{f_0}{BW}\left(\frac{1}{f_0} + \frac{f_0}{f^2}\right) \tag{2.11}$$

2.1.2 Bandpass filter electromagnetic formulation

Assuming lossless media of uniform dielectric constant and permeability within a structure of cylindrical symmetry and following the formalism of [15], it is possible to express the bandpass filter peak voltage or amplification factor (i.e. the voltage amplification in a resonator with respect to the input). Expressions for the peak electric field can then be obtained based on the voltage prediction.

In absence of reflection, the average power at the input waveguide of characteristic impedance Z_0 and cross section S is given by:

$$P_{in} = \frac{1}{2}\iint_S \left(\underline{E}\times\underline{H}^*\right)\cdot z_0 dS = \frac{1}{2}V(z)I^*(z)\iint_S \left(\underline{e}\times\underline{h}^*\right)\cdot z_0 dS = \frac{\left|\hat{V}_{in}\right|^2}{2Z_0} \tag{2.12}$$

The stored energy in the i-th physical resonator is obtained by integrating the dot product of the electric fields and the dot product of the magnetic fields over the resonator volume τ:

$$\begin{aligned} W_{ph,i} &= W_E + W_M = \frac{1}{4}\iiint_{volume}\left(\varepsilon\underline{E}\cdot\underline{E}^* + \mu\underline{H}\cdot\underline{H}^*\right)d\tau = \frac{1}{2}\iiint_{volume}\left(\varepsilon\underline{E}\cdot\underline{E}^*\right)d\tau \\ &= \frac{\varepsilon}{2}\left|\hat{V}_{ph,i}\right|^2\iint_A\left|\underline{e}\right|^2 dA\int_0^d \sin^2\left(k_z z\right)dz \equiv \frac{\varepsilon}{8}\left|\hat{V}_i^{res}\right|^2\lambda_{g0}l \end{aligned} \tag{2.13}$$

where l =1,..,n is the number of guided wavelengths associated to the operating resonant mode. Note that in equation (2.13) the orthogonality property is used, i.e.: the integration of the transverse electric field over the waveguide cross section A is equal to 1. The integral over the volume τ is decomposed into one surface integral over A and one line integral over z.

Equations (2.4), (2.5), (2.9) and (2.13) can be combined with the relevant transformation and solved for the peak voltage of the i-th resonator, obtaining the expression:

$$\hat{V}_i^{res} = \left|v_i\right|\sqrt{\frac{1}{\varepsilon\pi\lambda_{g0}l}\cdot\frac{dT}{df}} \tag{2.14}$$

The voltage amplification factor A_i for each resonator can be calculated combining (2.12) and (2.6):

$$A_i = \frac{\hat{V}_i^{res}}{\hat{V}_{in}} = \frac{\left|v_i\right|}{\left|v_0\right|}\sqrt{\frac{1}{\varepsilon\pi\lambda_{g0}lZ_0}\cdot\frac{dT}{df}} \tag{2.15}$$

which, in for TE_{nm} incident modes, can be rewritten as follows:

$$A_i = \frac{\hat{V}_i^{res}}{\hat{V}_{in}} = \frac{|v_i|}{|v_0|}\sqrt{\frac{c}{\pi\sqrt{\varepsilon_r}}\cdot\left(\frac{\lambda_0}{\lambda_{g0}^2 l}\right)\cdot\frac{dT}{df}} \tag{2.16}$$

Equations (2.15) and (2.16) show that the amplification factor is independent of the operating mode and thus of the filter geometry.

For a rectangular waveguide resonator with dimensions $a \times b \times d$ operating in the fundamental TE_{101} mode, the stored energy is calculated as:

$$W_{ph,i} = W_E + W_M = \frac{\varepsilon}{2}\int_0^d\int_0^b\int_0^a |\underline{E}|^2\, dxdydz \equiv \frac{\varepsilon}{8}\left|\hat{V}_i^{res}\right|^2 \lambda_{g0} \tag{2.17}$$

The maximum peak electric field for each resonator i for the fundamental mode TE_{101} is calculated combining (2.4), (2.5), (2.9) and (2.17):

$$\hat{E}_i^{res} = \hat{V}_i^{res}\sqrt{\frac{2}{ab}} = |v_i|\sqrt{\frac{2}{\varepsilon\pi ab\lambda_{g0}}\cdot\frac{dT}{df}} \tag{2.18}$$

For a circular waveguide resonator of radius a and length d, the stored energy for the fundamental mode TE_{111} is expressed as:

$$W_{ph,i} = W_E + W_M = \frac{\varepsilon}{2}\int_0^d\int_0^{2\pi}\int_0^a |\underline{E}|^2\, \rho d\rho d\varphi dz \equiv \frac{\varepsilon}{8}\left|\hat{V}_i^{res}\right|^2 \lambda_{g0} \tag{2.19}$$

The maximum peak electric field for each (electrical) resonator i for the fundamental mode TE_{111} is calculated (2.4), (2.5), (2.9) and (2.17):

$$\hat{E}_i^{res} = \hat{V}_i^{res}\frac{2}{3a} = |v_i|\frac{1}{3a}\sqrt{\frac{2c}{\pi\sqrt{\varepsilon_r}}\cdot\left(\frac{\lambda_0}{\lambda_{g0}^2 l}\right)\cdot\frac{dT}{df}} \tag{2.20}$$

For a coaxial resonator of outer radius a, inner radius b and length d, the stored energy for the fundamental TEM mode is obtained as follows:

$$\begin{aligned} W_{ph,i} &= W_E + W_M = \frac{\varepsilon}{2}\int_0^d\int_0^{2\pi}\int_b^a |\underline{E}|^2\, \rho d\rho d\varphi dz \\ &= \frac{\varepsilon}{2}\int_0^d\int_0^{2\pi}\int_b^a \frac{\left|\hat{V}_{N,i}\right|^2}{\rho^2\ln^2(a/b)}\sin^2\left(\frac{\pi}{d}z\right)\rho d\rho d\varphi dz \equiv \frac{\varepsilon\left|\hat{V}_{N,i}\right|^2\lambda_{g0}\pi}{4\ln(a/b)} \end{aligned} \tag{2.21}$$

where the voltage is normalized here as defined in [14]:

$$\hat{V}_{N,i} = \frac{\hat{V}_i^{res}}{\sqrt{N}} = \frac{\hat{V}_i^{res}}{\sqrt{\frac{\ln(a/b)}{2\pi}}} \tag{2.22}$$

Equations (2.4), (2.5), (2.9) and (2.19) can be combined and solved for the peak voltage of the *i*-th resonator, obtaining the expression:

$$\hat{V}_{N,i} = |v_i| \sqrt{\frac{\ln(a/b)}{2\varepsilon\pi^2\lambda_0} \cdot \frac{dT}{df}} \tag{2.23}$$

The maximum peak electric field for each resonator can then be calculated as follows:

$$\hat{E}_i^{res} = \frac{\hat{V}_{N,i}}{b\ln(a/b)} \tag{2.24}$$

It is worth noting that (2.15) and (2.16) can be found again dividing the peak resonator fields by the peak field at the input waveguide, for each of the cases studied. This is once again in agreement with the previous result on the amplification factor independence of geometry. Numerical and experimental validation of the theory applied to the rectangular waveguide case is reported in [7].

Novel explicit formulas are also derived for the case of evanescent-mode filters in ridge waveguide. Introducing the factor $\Delta=2/(1+1/(1-(\lambda_c/\lambda_0)^2))$ to account for the steeper slope-parameters of evanescent-mode sections with respect to lumped elements [16] and including the impedance ratio of the matching network, (2.4), (2.5), (2.10) and (2.13) are combined to obtain:

$$\hat{V}_i(f) = |v_i| \sqrt{\frac{2\Delta}{\varepsilon\pi\lambda_{g0}} \cdot \frac{Z_i}{Z_0} \cdot \frac{f_0}{BW}\left(\frac{1}{f_0} + \frac{f_0}{f^2}\right)} \tag{2.25}$$

where v_i is the peak voltage calculated from the prototype, λ_{g0} is the guided wavelength calculated at center frequency, Z_i and Z_0 are the characteristic impedances of the *i*-th ridge section and input rectangular waveguide respectively.

2.1.3 Example: C-Band ridge waveguide filter

A C-Band ridged filter (n = 4, RL = –24 dB, f_0 = 6 GHz, BW = 570 MHz) is analysed with the new formula (2.25) as well as the FDTD method (Fig. 2-2). Voltage monitors are placed in the EM model at the middle of ridge waveguide sections, where the maximum homogeneous field occurs. Comparison between analytical and numerical results in terms of peak voltage (for 1 W input peak power) are summarized in Fig. 2-3. Very good agreement is obtained.

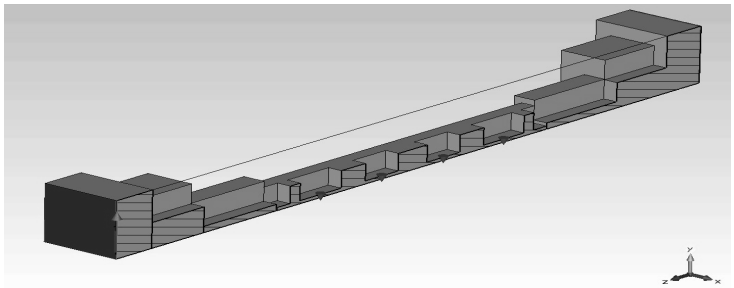

Fig. 2-2: 3D view (E-plane half cut) of the evanescent-mode ridge waveguide filter example. The critical gaps have all identical size and impedance (Z_i=76.1 Ω at f_0). The input characteristic impedance is Z_0=490.3 Ω at f_0.

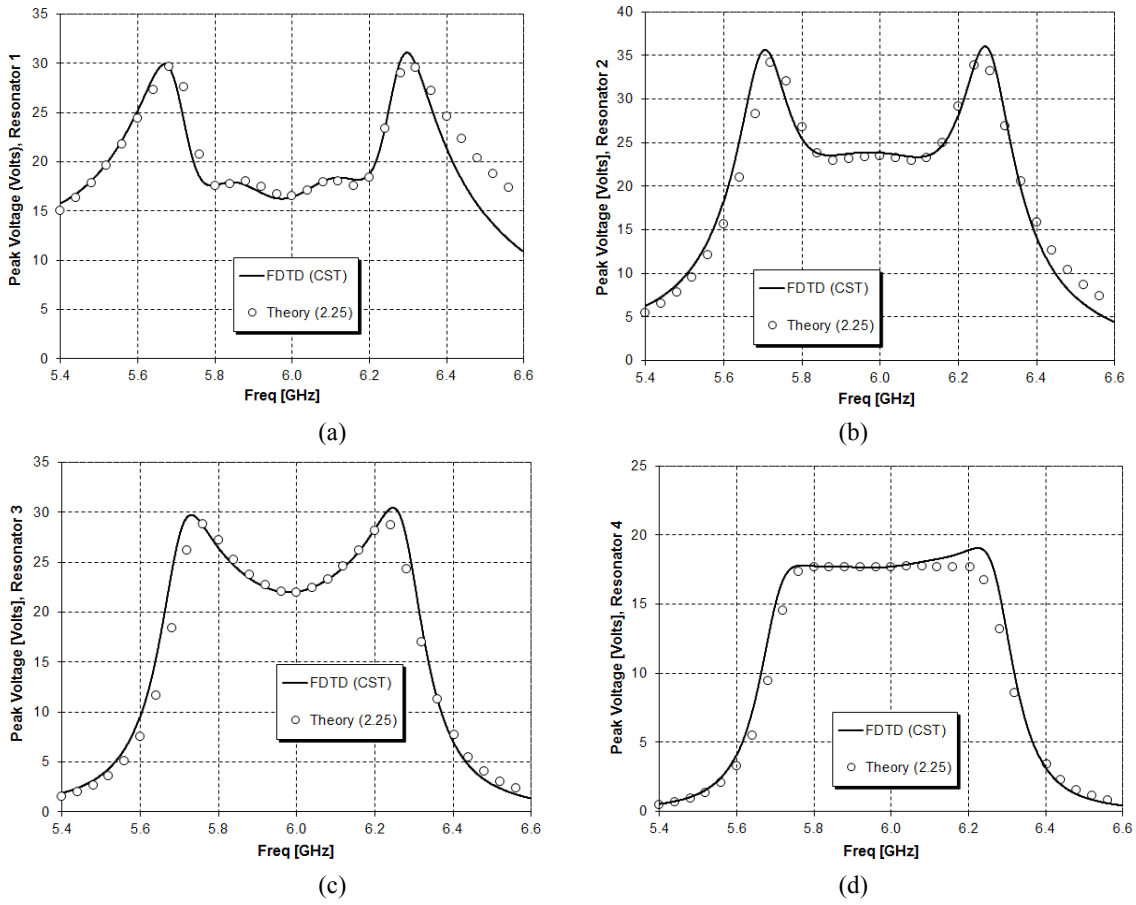

Fig. 2-4: Peak voltage along the center line of the filter critical regions using FDTD and comparison of the values obtained using theory (2.25). (a) Resonator 1; (b) Resonator 2; (c) Resonator 3; (d) Resonator 4.

2.2 Voltage prediction in stepped-impedance low-pass filters

Many applications use high-Q and narrow-band filters characterized by high voltage amplification, i.e.: the internal resonator voltages are significantly higher than input value. Previous works therefore focused on analysis techniques for predicting the power handling capability of bandpass filter structures, where the problem is solved by analysing a lumped prototype circuit with appropriate scaling factors. Common objective of previously reported methods is to simplify power handling predictions, either reducing [16], [17] or eliminating [18], [19] the use of full-wave simulations. Although a large amount of reference material is available for bandpass filters, very limited information is found in case of low-pass filters. This can be explained by two facts: 1) the vast majority of applications require bandpass filters with narrow bandwidths (~1%); 2) low-pass filters are typically low-Q devices with low voltage amplification. In [1] it is indeed stated: *"...For very wideband filters (>20%), the same voltage value as at the input may be directly used inside filters due to low voltage amplification*".

Empirical assumptions on the voltage amplification appear too simplistic for low-pass filters found in modern applications. On one side, there is constant demand for higher power low-pass filters, for both single-carrier and multi-carrier operation. On the other side, increasingly stringent

stop band requirements lead to small-gap microwave structures. Both trends increase in parallel the low-pass filters risk of multipactor and dielectric breakdown. Typical examples include the output multiplexer harmonic filters and transmit filters integrated into antenna feed systems. Today's high performance communication systems therefore push the technical requirements of low-pass filters, up to the point where accurate estimation of their power handling capability becomes a priority. Even a relatively small inaccuracy in the voltage prediction introduces an error in the power handling assessment, which could lead to unnecessary design iterations or test campaigns.

Currently, precise analysis of the field/voltage distribution in low-pass filters requires rigorous electromagnetic (EM) modeling, using either modal analysis [20], [21] or numerical techniques such as the Finite Element Method (FEM) or the Finite Difference Time Domain (FDTD) method [22]. EM modeling is time consuming and requires detailed design dimensions of the overall structure.

Novel explicit formulas are introduced in this work for the prediction of peak voltages and amplification factors in stepped-impedance coaxial and waveguide low-pass filters. Only network prototype parameters – rather than 3D EM simulations – are required in this method, which is therefore fast and considerably simplifies the power handling analysis of low-pass filter networks.

2.2.1 Low-pass filter frequency transformation

Two main classes of low-pass prototype filters have been previously reported: the distributed stepped-impedance filter [23] and the mixed lumped/distributed filter [24]. Both filter types use commensurate transmission lines as essential building blocks. Commensurate elements are short lines of identical physical length d and electrical length $\theta=\beta d$. The line impedance has frequency dependency of the form $t=j\tan\theta$ as compared to $s=j\omega$ of lumped elements. At a given commensurate frequency, $\theta_c=\beta d|_{\omega=\omega c}=\omega_c d/v_p$ where v_p is the phase velocity. Therefore the electrical length can be expressed as [25]:

$$\theta = \beta d = \frac{\omega d}{v_p} \approx \frac{\omega}{\omega_c}\theta_c = \frac{f}{f_c}\theta_c \tag{2.26}$$

The frequency transformation in the (distributed) low-pass case is:

$$T(f) = \omega' = \frac{\sin\theta}{\sin\theta_c} \tag{2.27}$$

where θ_c is the commensurate electrical length (or cut-off angle), set as the desired filter cut-off frequency f_c.

Substituting (2.26) into (2.27), the derivative of transformation T with respect to frequency is calculated as:

$$\frac{dT}{df} = \frac{1}{\sin\theta_c}\cdot\frac{\theta_c}{f_c}\cos\left(\frac{f}{f_c}\theta_c\right) \tag{2.28}$$

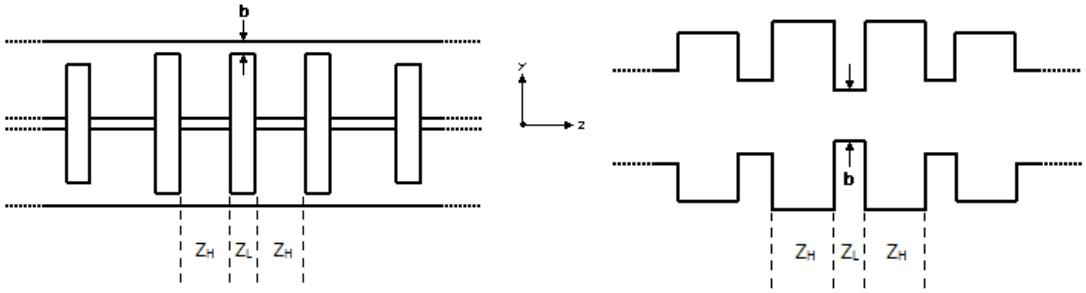

(a) (b)

Fig. 2-5: Generic capacitive section as critical element of high power stepped-impedance filters (cross-section) (a) Coaxial realization; (b) Waveguide realization..

2.2.2 Low-pass filter electromagnetic formulation

A generic commensurate element of low characteristic impedance Z_L, connected at both ends to high characteristic impedance levels Z_H is indicated in Fig. 2-5(a) (coaxial) and Fig. 2-5(b) (waveguide). Focus is on a critical gap b susceptible to RF voltage breakdown. The following conditions are normally verified in practical designs: 1) $Z_H >> Z_L$, i.e., the tangential component of the magnetic field is close to zero at the discontinuity; 2) each length d is shorter than $\lambda_g/10$. Thus the generic low-impedance element is approximated by a lumped capacitor:

$$C_{ph} \approx \frac{1}{2\pi f Z_L}\tan(\beta d) = \frac{1}{2\pi f Z_L}\tan\left(\frac{f}{f_c}\theta_c\right) \approx \frac{1}{2\pi f Z_L}\cdot\frac{f}{f_c}\theta_c = \frac{\theta_c}{2\pi f_c Z_L} \tag{2.29}$$

The stored energy of a capacitive physical section is then expressed analytically as:

$$W_{ph} = W_E + W_M = \frac{1}{4}\iiint_{volume}\left(\varepsilon\underline{E}\cdot\underline{E}^* + \mu\underline{H}\cdot\underline{H}^*\right)d\tau \approx \frac{1}{4}C_{ph}\hat{V}_{ph}^{\ 2} = \frac{\theta_c}{8\pi f_c Z_L}\hat{V}_{ph}^{\ 2} \tag{2.30}$$

At the filter input waveguide of cross section S and characteristic impedance Z_0, the average power is given by:

$$P_{in} = \frac{1}{2}\iint_S\left(\underline{E}\times\underline{H}^*\right)\cdot z_0 dS = \frac{1}{2}V(z)I^*(z)\iint_S\left(\underline{e}\times\underline{h}^*\right)\cdot z_0 dS = \frac{\left|\hat{V}_{in}\right|^2}{2Z_0} \tag{2.31}$$

2.2.3 Correspondence between model and physical structure

The stepped-impedance filter structure is realized as a cascade of n+2 waveguide or coaxial sections, which are the physical implementation of alternate high and low characteristic impedance transmission lines. All lines are small compared to quarter-wavelength at *pass-band* frequencies. Inspection of (2.29) suggests in fact that the small-angle approximation is valid for all frequencies equal or below f_c (i.e., all frequencies of the low-pass filter pass-band). The lumped element model of Fig. 2-1 is then a fairly accurate representation of the physical structure in the frequency range of interest for voltage and power-handling predictions. Equations (2.4), (2.5), (2.28) and (2.30) can be combined and solved for the peak voltage in the i-th capacitive section:

$$\hat{V}_i^{cap} = |v_i| \sqrt{\frac{\cos\theta}{\sin\theta_c} \cdot Z_i} \tag{2.32}$$

where v_i is the peak voltage calculated from the direct-coupled prototype, θ_c is the specified cut-off angle and Z_i is the characteristic impedance of the i-th capacitive section.

Imposing the equivalence between the input powers in the circuit and electromagnetic models, the peak voltage in the input waveguide can be expressed as::

$$\hat{V}_{in} = |v_0| \sqrt{Z_0} \tag{2.33}$$

The voltage amplification factor A_i [20]–[22] is obtained from (2.32) and (2.33) for any i-th capacitive section:

$$A_i(f) = \frac{\hat{V}_i^{cap}}{\hat{V}_{in}} = \frac{|v_i|}{|v_0|} \sqrt{\frac{\cos\theta}{\sin\theta_c} \cdot \frac{Z_i}{Z_0}} \tag{2.34}$$

2.2.4 Example: UHF coaxial low-pass filter

A UHF coaxial low-pass filter (n=9, RL=–22 dB, θ_c=22.5°, f_c=800 MHz, Z_0=50 Ω) was designed using the mixed lumped/distributed prototype method [24]. The filter consists of an inner conductor with short disks of diameter d_i, inserted within an outer conductor of constant diameter D (Fig. 2-6). The capacitive sections are completely filled with a sleeve of dielectric material (ε_r=2.3) for mechanical and thermal reasons. Dielectric breakdown is therefore the limiting factor for such filters under high-power operation.

The overall structure was simulated with FDTD numerical techniques (CST Microwave Studio). Voltage results from CST were compared with values from the new formula, which for the coaxial case assumes the explicit form:

$$\hat{V}_i^{cap}(f) = |v_i| \sqrt{\frac{\cos\theta}{\sin\theta_c} \cdot \frac{1}{2\pi} \sqrt{\frac{\mu_0}{\varepsilon_0 \varepsilon_r}} \cdot \ln\left(\frac{D}{d_i}\right)} \approx |v_i| \sqrt{\frac{\cos\theta}{\sin\theta_c} \cdot \frac{138}{\sqrt{\varepsilon_r}} \cdot \log b_i} \tag{2.35}$$

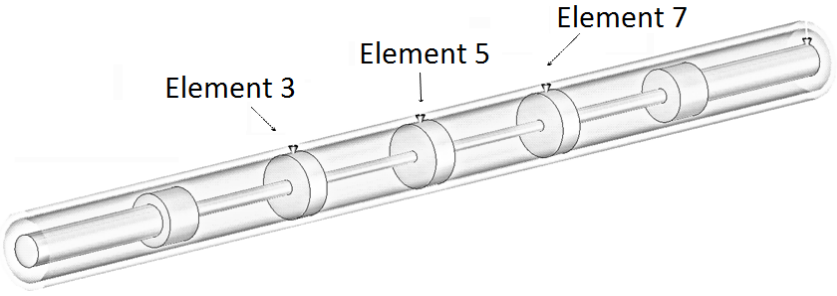

Fig. 2-6: 3D view of the coaxial low-pass filter design example. The critical gaps indicated have all identical size (D=23 mm, d_i=18.63 mm). The input characteristic impedance is Z_0=50 Ω.

where b_i is the ratio between outer and inner conductors for the i-th capacitive section.

Predicted peak voltages using the two analysis methods (for 1 W input peak power) are reported in Fig. 2-7. The agreement is good in the pass-band range and nearly exact in proximity of the filter cut-off frequency, where the maximum voltage occurs. As expected, the theory diverges from numerical results for out-of-band frequencies.

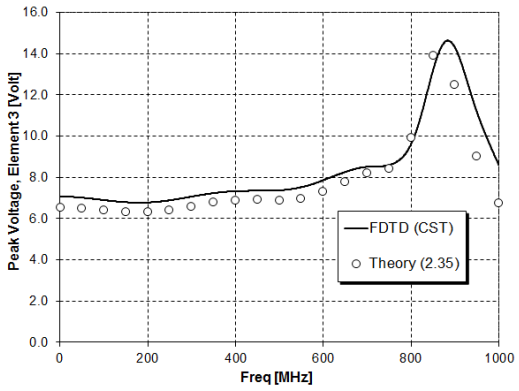

(a)

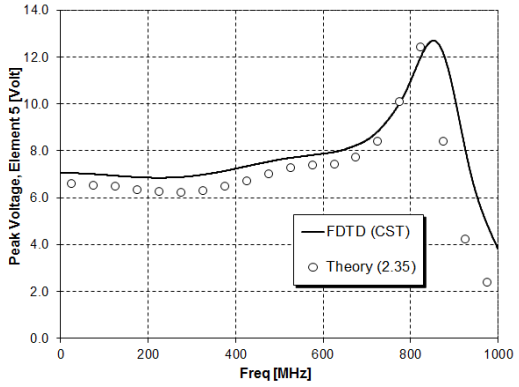

(b)

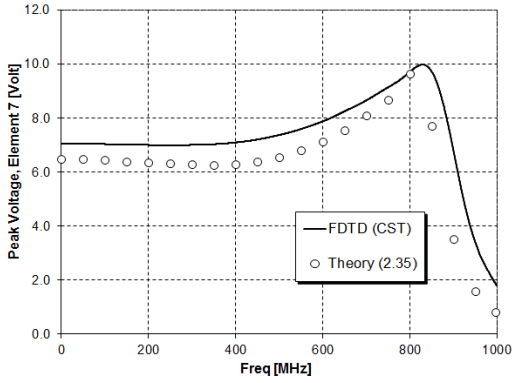

(c)

Fig. 2-7: Voltage amplification factors along the center line of the filter critical regions using FDTD and comparison of the values obtained using theory (2.35). (a) Element 3; (b) Element 5; (c) Element 7.

2.2.5 Example: Ku-Band waveguide low-pass filter

A Ku-Band waveguide low-pass filter (n=9, RL=-35 dB, θ_c=30°, f_c=12 GHz) was designed using the stepped-impedance prototype method [23]. The filter is realized as an E-plane rectangular corrugated waveguide of constant width a, input section of height b_0 and small-gap capacitive sections of height b_i. Multipactor is normally the limiting factor for high-power waveguide low-pass filters operating in vacuum.

The amplification factors in the critical elements (Fig. 2-8) were calculated using CST Microwave Studio as well as with the new formula in the explicit form:

$$A_i(f) = \frac{\hat{V}_i^{cap}}{\hat{V}_{in}} = \frac{|v_i|}{|v_0|}\sqrt{\frac{\cos\theta}{\sin\theta_c}\cdot\frac{b_i}{b_0}} \tag{2.36}$$

Results are plotted for comparison in Fig. 2-9, where again, there is a close correlation between numerical and analytical results from (2.36). From the obtained A_i values, the multipactor threshold is estimated for the worst-case (Element 5) using the formula:

$$P_{th}(f) = \frac{V_{th}^{\ 2}}{2Z_0 A_5(f)^2} \tag{2.37}$$

where V_{th} is the theoretical peak voltage threshold for parallel-plate structures [26] and Z_0 is the input impedance according to the power-voltage definition. Note that the parallel-plate model is a valid assumption in this case, considering the small gap-to-length ratio of this example where fringing field effects do not affect the breakdown threshold [27].

The filter was manufactured of aluminium, silver-plated and high-power tested in vacuum up to the breakdown (Fig. 2-10). Predicted and measured results are summarized in Table 2-1, where good agreement is reported. The difference between analysis and test results is within the set-up measurement accuracy of ±1 dB. It is interesting to note how the use of conventional circuit models or common engineering assumptions (i.e., A_i=1) would have introduced a significant error in the power handling prediction. The former approach would lead to a calculated threshold of 370 W (about 3 dB underestimation), the latter would give a threshold value of 1500 W (about 3 dB overestimation).

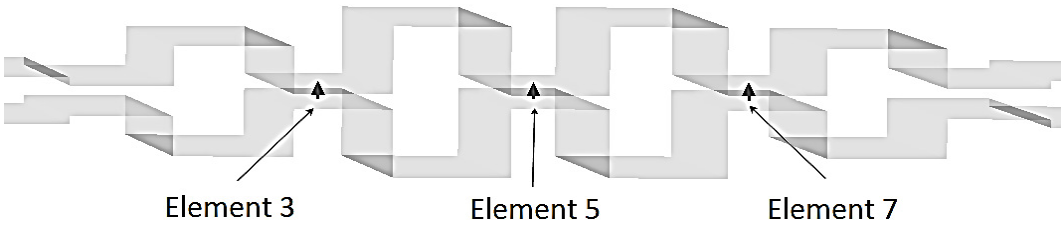

Fig. 2-8: 3D view of the waveguide low-pass filter example, where the areas of interest for voltage calculation are indicated. The critical gap is Element 5 (b5=0.27 mm). The input waveguide height is b_0=1.028 mm.

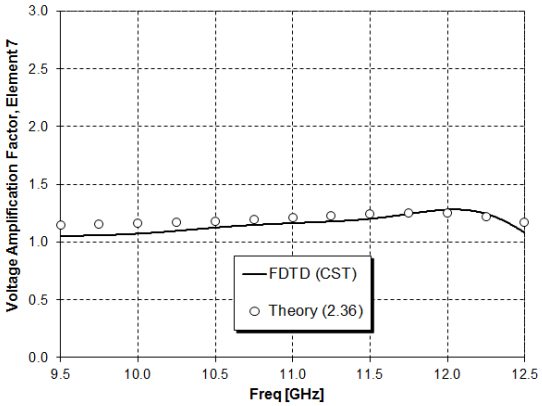

(a)

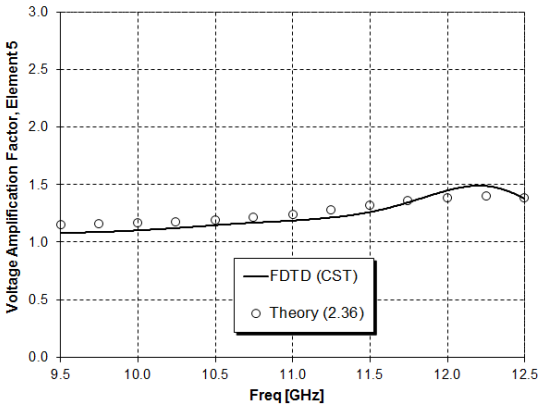

(b)

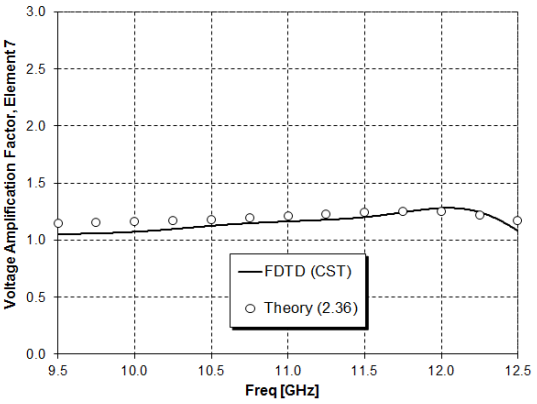

(c)

Fig. 2-9: Voltage amplification factors along the centre line of the filter critical regions using FDTD and comparison of the values obtained using theory (16). (a) Element 3; (b) Element 5; (c) Element 7.

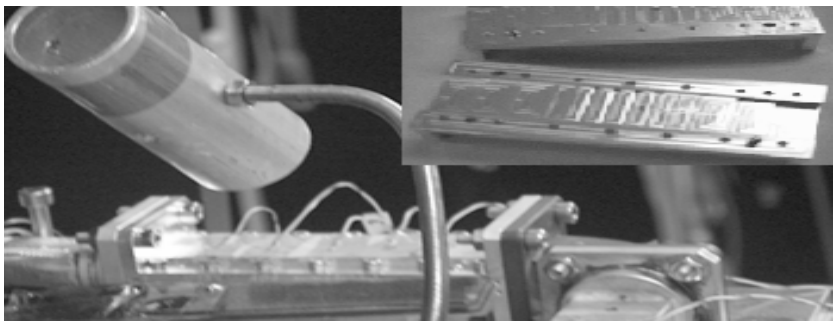

Fig. 2-10: Ku-Band waveguide filter and experimental test set-up.

TABLE 2-1
KU-BAND FILTER MULTIPACTOR SUMMARY

Unit	Parameter	Value	Notes
GHz	Frequency	11.8	
mm	Gap size	0.27	Worst-case region (b_5)
V	Breakdown voltage (peak)	400	Theoretical value for Ag surface finish [26]
-	Amplification factor (A_5)		
	- Calculated with (2.36)	1.35	
	- Calculated with CST	1.37	
W	Multipactor threshold		
	- Predicted using (2.36) and (2.37)	800	
	- Predicted using CST and (2.37)	775	
	- Measured	950	

2.2.6 Example: design charts

The analytical equations introduced find use also in the optimization of low-pass filters power handling capability. Design charts are readily generated from a given voltage breakdown law in combination with (2.32) or (2.34), expressing the power threshold as a function of the gap size (or impedance) of the critical filter elements.

As an example, considering the previous Ku-Band specifications and knowing the multipactor design boundary for silver-plated RF hardware [26]:

$$V_{th,i} = 63 \cdot f[GHz] \cdot b_i[mm] \tag{2.38}$$

the susceptibility power threshold is expressed combining (2.36), (2.37) and (2.38) as follows:

$$P_{th}(f) = \min_i \left\{ \frac{1}{2Z_i} \cdot \frac{\sin\theta_c}{\cos\theta} \cdot \left(\frac{v_0}{v_i} \cdot 63 f b_i \right)^2 \right\} \tag{2.39}$$

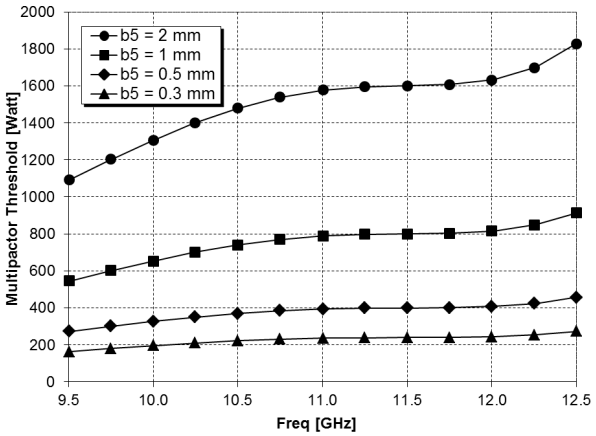

Fig. 2-11: Design chart expressing the multipactor threshold for different gap sizes of the critical filter element.

From (2.39), power breakdown curves for the critical element are plotted for several gap sizes (Fig. 2-11). Advanced features such as safety margins and correction factors for geometry can be included to generate enhanced design charts. The same approach can be adopted for breakdown mechanisms of other type, using the respective physical law.

2.3 Discussion and limitations

The method presented for the bandpass filter case provided very good predictions of the maximum peak electric field and the frequency at which the peak occurs. Considering all cases analysed here and in [7], the error made is less than 7% in the prediction of the electric field with respect to numerical simulations, and less than 5.5% with respect to measurements. The error made in the prediction of the related frequencies is less than 0.2%. The errors introduced are due to the following assumptions made in the theory:

- Moderate band filters (up to 20%) whose transfer function is well represented by the selected frequency transformation
- Frequency transformation valid for a given coupling element (shunt inductive or evanescent-mode) – however the theory is still valid when suitable frequency transformation are assumed
- Stored energy calculated at centre frequency – this is slightly different at the band-edge frequencies where the maximum field occurs

The above limitations do not jeopardize the prediction results that are considered very good for practical applications.

In the low-pass case, examples show very good agreement between analytical and numerical simulations near the cut-off frequency. For lower pass-band frequencies, the correlation with numerical results is still good but not exact. It is believed that the difference (less than 10% in all cases analysed) is due to the following approximations:

- the conditions imposed on the impedance and length of the filter elements
- the fringing capacitances ignored in the resulting explicit formulas
- the interaction between discontinuities, more significant for lower pass-band frequencies.

As the frequency range of interest is usually near or below the filter cut-off, the accuracy of the formulas derived is considered satisfactory for practical applications.

One limitation of the proposed approach is the homogeneous field assumption. This does not allow discontinuities or field singularities in the critical sections. When calculating RF power thresholds, there could exist conditions for local breakdown, even if the peak voltage is below a given theoretical threshold. However, when the breakdown nature is known and a parallel-plate model is applicable (which can often be the case), this is not a limitation anymore.

2.3.1 Multipactor

Multipactor analysis requires voltage values in order to calculate power thresholds and margins. For a given gap size, the effect of fringing fields at discontinuities is to increase the breakdown voltage with respect to the parallel-plate model. Such an effect is negligible when the waveguide height is much smaller than length (i.e., $b/d<1$, as demonstrated in the Ku-band example of this chapter) and becomes more important for larger aspect rations (i.e., $b/d \geq 1$). The latter case can still be analysed with the homogeneous field approach of this method if appropriate correction factors for geometry are applied to voltage threshold [27] or susceptibility regions [28].

2.3.2 Ionization and dielectric breakdown

Contrary to the multipactor, ionization and dielectric breakdown are characterised by a more localized effect, therefore the contribution of field singularities becomes extremely important. The critical case of tuning screws can be ruled out, as broadband filters today are fabricated without any post-production tuning. Special attention is however necessary for the capacitive steps, where high field enhancements occur near inductive areas of much lower field.

When diffusion is the main electron loss mechanism, such corner effects do not normally generate ionization breakdown as electrons can freely move to low-field regions. Several inductive and corrugated filter examples can be found in [29], where numerical and experimental results are reported. For all cases studied, the breakdown develops in homogeneous field regions, across the inner gaps full height. Since waveguide steps are not a concern in the determination of breakdown levels, the proposed method is expected to provide accurate predictions when diffusion dominates. This covers the important case of gas breakdown at low and intermediate pressure range (including critical pressure).

When attachment is the main electron loss mechanism, the breakdown normally occurs in proximity of corners as the diffusion region is limited. There exists a risk of error in the threshold prediction, due to the electric field singularity not considered in this method. Typical case is air breakdown at atmospheric pressure. However the physics of such phenomena is much more complex than other breakdown types; hence, numerical analysis or experimental validation often cannot be avoided anyhow. In similar instances, this method could still be used for rough analysis, e.g., to obtain starting values in numerical simulations of gas breakdown. Another interesting case could be when rounded corners are employed in the design so that field singularities do not contribute to the breakdown onset.

2.4 Summary

An analytical method for the prediction of peak voltages, peak electric fields and/or amplification factors in bandpass and low-pass filters has been introduced in this chapter. It is shown that the method is general and not restricted to filter topology or detailed design dimensions, as a result of the coupling matrix and electromagnetic formulations used in tandem. Under certain conditions, this method can be employed for fast and accurate power handling predictions, without need of 3D EM simulations of the overall filter structure.

For bandpass filters, the method is based on the concept of the stored energy in waveguide resonators and an equivalent low-pass prototype network using accurate frequency transformations valid for inductive irises or evanescent waveguide sections. Introducing relevant coupling elements in (2.2) would allow handling arbitrarily complex transfer functions (e.g., elliptic). Similarly, replacing the frequency transformation T in equation (2.5) would allow representing different coupling elements (e.g. capacitive).

Equally general is the approach introduced for stepped-impedance low-pass filters, which can be extended to other filter functions (e.g. Zolotarev), or types (e.g. waffle-iron). Only prototype network parameters are required, i.e.: coupling matrix, cut-off angle and impedance levels of the critical sections. The formulas have been verified via FDTD simulations on coaxial and waveguide examples, as well as via multipactor breakdown test on a waveguide filter breadboard. Simulation and measurement results also show how the use of conventional circuit models or empirical

assumptions on the voltage amplification could lead to a significant error in the power threshold computation.

Being network-based, this method is fast and can be adopted at any step of the filter design process. The following application scenarios are thus envisaged:

- As analysis tool to simplify the prediction of power handling capability of an existing filter design
- As design tool to assist in power handling optimization and trade-offs in early stages of the low-pass filters design.

2.5 References

[1] M. Yu, "Power-Handling Capabilities of RF filters," IEEE Microwave Magazine, October 2007.

[2] "Multipaction design and test," European Space Agency, Noordwijk, The Netherlands, ECSS-E-20-01A, May 5, 2003.

[3] "The study of multipaction breakdown in space electronic systems," Hughes Aircraft Company, Culver City, CA, USA, NASA Report CR-448, contract NAS 5-3916.

[4] J. Puech, M. Merecki, D. Anderson, M. Buyanova, D. Doroshkina, U. Jordan, L. Lapierre, M. Lisak, V.E. Semenov, J. Sombrin, and R. Udilijak, "Microwave discharge research activities within the contest of the Chalmers University (Sweden)/Institute of Applied Physics (Russia)/CNES (France) project," in Proc. 4th Int. Workshop on Multipactor, Corona and Passive Intermodulation in Space RF Hardware (MULCOPIM 2003), ESTEC, Noordwijk, The Netherlands, Sep. 2003.

[5] H.C. Bell, "The coupling matrix in low-pass prototype filters," IEEE Microwave Magazine, Apr. 2007.

[6] G. Schettini, Editor, Advanced Techniques for Microwave Systems, Kerala, India: Research Signpost, 2011, Chapter 6 (D. Schmitt and F. M. Vanin, RF Waveguide Filters Design Guidelines).

[7] F. M. Vanin, "Waveguide bandpass filters and diplexers – analysis and synthesis," Ph.D. dissertation, Sapienza Univ., Rome, Italy, May 2012.

[8] C. Ernst and V. Postoyalko, "Comparison of the stored energy distribution in a QC-type and a TC-type prototype with the same power transfer function," in IEEE MTT-S Int. Microwave Symp. Dig., June 1999, vol. 3, pp. 1339–1342.

[9] L. Young, "Peak internal fields in direct-coupled-cavity filters," IEEE Trans. Microwave Theory Tech., vol. 8, no. 6, pp. 612–616, 1960.

[10] A. Sivadas, M. Yu, and R.J. Cameron, "A simplified analysis for high power microwave bandpass filter structures," in Proc. Int. Symp. IEEE Microwave Theory and Techniques, Boston, MA, June 2000, vol. 3, 2000, pp. 1771–1774.

[11] A. R. Harish and R.J. Cameron, "Peak voltage analysis in high power microwave filters," in Proc. IEE Colloquium Microwave Filters and Multiplexers, Nov. 2000, pp. 10/1-10/5.

[12] C. Ernst and V. Postoyalko, "Prediction of peak internal fields in direct-coupled-cavity filters," IEEE Trans. Microwave Theory Tech., vol. 51, no. 1, pp. 64–73, Jan. 2003.

[13] R. Levy, "Theory of Direct Coupled Cavity Filters," IEEE Trans. Microwave Theory and Tech., vol. 11, pp. 340-348, June 1967.

[14] G. F. Craven and C. K. Mok, "The Design of Evanescent Mode Waveguide Bandpass Filters for a Prescribed Insertion Loss Characteristic," IEEE Trans. Microwave Theory & Tech., vol. 19, no. 3, pp. 295-308, March 1971.

[15] N. Marcuvitz, Waveguide Handbook, Boston Technical Publishers, Inc., 1964.

[16] A.R. Harish and R.J. Cameron, "Peak voltage analysis in high power microwave filters," in Proc. IEE Colloquium on Microwave Filters and Multiplexers, pp. 10/1-10/5, Nov. 2000.

[17] C. Wang and K. Zaki, "Analysis of power handling capacity of band pass filters," IEEE MTT-S Int. Microwave Symp. Dig., May 2001, vol. 3, pp. 1611–1614.

[18] A. Sivadas, M. Yu, and R.J. Cameron, "A simplified analysis for high power microwave bandpass filter structures," in Proc. Int. Symp. IEEE Microwave Theory and Techniques, Boston, MA, June 2000, vol. 3, 2000, pp. 1771–1774.

[19] C. Ernst and V. Postoyalko, "Prediction of peak internal fields in direct-coupled-cavity filters," IEEE Trans. Microwave Theory Tech., vol. 51, no. 1, pp. 64–73, Jan. 2003.

[20] M. Ludovico, L. Accatino, G. Zarba, and M. Mongiardo, "CAD of Multipactor–free Waveguide Components for Communication Satellites," IEEE MTT-S Digest, June 2002, pp. 2077 – 2080.

[21] I. Arregui, S. Anza, I. Arnedo, C. Vicente, A. Lujambio, J. Gil, M. Chudzik, B. Gimeno, T. Lopetegi, M. A. G. Laso, and V. E. Boria, "Multipactor prediction in novel high-power low-pass filters with wide rejection band," in Proc. 39th European Microwave Conference, Rome, Italy, 29 Sept. – 1 Oct. 2009, pp. 675-678.

[22] P. Sarasa, A. Gonzalez, H. Esteban, P. Mader, K. Tossou, P. Lepeltier, "Comparative study of the power handling capability of space broadband antenna filters in Ku-Band," in Proc. 5th Int. Workshop on Multipactor, Corona and Passive Intermodulation in Space RF Hardware, ESTEC, Noordwijk, The Netherlands, Sept. 2005.

[23] R. Levy, "Tables of element values for the distributed low~pass prototype filter," IEEE Trans. Microwave Theory Tech., MTT-13, no. 5, Sept. 1965, pp. 514-536.

[24] R. Levy, "New class of distributed prototype filters with applications to mixed lumped/distributed component design", IEEE Trans. Microwave Theory Tech., MTT-18, no. 12, Sept. 1970, pp. 1064-1071.

[25] R.J. Cameron, C.M. Kudsia, and R.R. Mansour, Microwave Filters for Communication Systems: Fundamentals, Design and Applications. New York: Wiley 2007.

[26] A. Woode and J. Petit, "Diagnostic investigations into the multipactor effect, susceptibility zone measurements and parameters affecting a discharge," European Space Agency, Noordwijk, The Netherlands, ESTEC Working Paper 1556, Nov. 1989.

[27] D. Wolk, C. Vicente, L. Hartnagel, M. Mattes, J. R. Mosig, and D. Raboso, "An investigation of the effect of fringing fields on multipactor breakdown," in Proc. 5th Int. Workshop Multipactor, Corona and Passive Intermodulation in Space RF Hardware, ESTEC, Noordwijk, The Netherlands, Sept. 2005.

[28] R. Udiljak, D. Anderson,M. Lisak, J. Puech, and V. E. Semenov, "Multipactor in a waveguide iris," IEEE Trans. Plasma Sci., vol. 35, no. 2, pp. 388–395, Apr. 2007.

[29] C. Vicente, "Passive intermodulation and corona discharge for microwave structures in communications satellites," Ph.D. dissertation, Inst. Hochfrequenztech., Technical Univ. Darmstadt, Darmstadt, Germany, 2005.

Chapter 3. Design of high-performance broadband filters

The trend towards performance improvement finds a relatively solid ground in the space passive RF domain. One reason is the lower risk (compared to active equipment for example) perceived by satellite operators in introducing new RF technologies. This trend is clearly visible in the (narrowband) IMUX/OMUX area. Dielectric materials, temperature compensation techniques and novel high-Q cavity resonators are examples of key technologies enabling significant improvements in terms of hardware miniaturization, power increase and loss reduction. Surprisingly, a similar trend is not found in (broadband) output section equipment, where conservative and non-optimal solutions are still widely encountered.

Splitting of broadband signals still employs conventional H-plane TE_{10n} mode diplexers (in some applications, tri-/quadruplexers are used), representing a bottle-neck in the performance versus development effort trade-off.

Low-pass harmonic filters are still based on old-fashioned design concepts deriving from studies of the seventies. Failure in meeting requirements of future space applications is the limitation in this case.

3.1 Ka-Band waveguide diplexer with engineered layout

While Ka-band frequencies become more and more attractive for broadband telecommunication systems, design and manufacturing of waveguide components for Ka-band is more demanding and requires a higher degree of precision than lower frequencies. An example is the antenna feed chain of terrestrial or space systems (feedhorn, polarizer, ortho-mode transducers, and transmit/receive filtering), where the diplexer represents a significant part of the development time and cost. The design drivers in such diplexer applications are: a) low return loss; b) optimal Electromagnetic Compatibility (EMC) performance; c) low Passive Intermodulation Products (PIM) generation; d) low cost. In order to balance out all these factors against the desired design and cost goals, it is recommended to adopt ingenious design concepts, allowing efficient Electromagnetic (EM) modeling and precise fabrication without need of post-production tuning or adjustments.

A compact and elegant design approach is presented in this chapter, addressing the above mentioned challenges. Figure 1 shows the 3D view of the diplexer structure together with the top view. The diplexer body is realized using a single-piece metal structure which combines a monolithic junction (bifurcation) and the two filter arms. Interresonator couplings are realized by inductive windows asymmetrically located along each filter. H-plane symmetry is therefore maintained for the overall diplexer. Finally, two flat metal plates are mated to the body sides, closing the structure providing optimal contact among metal parts.

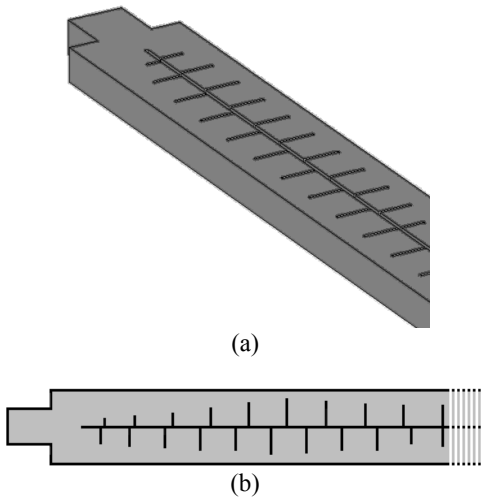

Fig. 3-1: Diplexer layout. (a) 3D view; (b) Top view.

3.1.1 Layout description and advantages

Previous studies focused on different H-plane and E-plane three-port junctions [1]-[5], each presenting specific advantages and disadvantages. Preference is typically for diplexer designs which are manufactured in two identical parts and then assembled along the broad waveguide dimension, ensuring low electrical current across the interface. For this reason an E-plane T-junction is often chosen to combine two inductive iris filters, but this approach still suffers of two major limits: computational inefficiency – due to the lack of EM symmetries – and noticeable production time and cost – due to the strong dependency on manufacturing standards. All these considerations become critical for Ka-band applications, where more stringent mechanical requirements are faced due to the small wavelength.

The design approach proposed here uses an H-plane bifurcation connected to inductive iris filters, where asymmetric windows realize the required couplings between rectangular cavity resonators. As compared to conventional designs, the proposed layout provides advantages from both computational and manufacturing viewpoints. Due to the properties of the H-plane symmetry, for Mode Matching (MM) techniques only TE_{n0} modes are computed, whereas in case of Finite Element Method (FEM) the number of cells analysed can be significantly reduced. The diplexer layout allows the fabrication of the junction and filters body and irises in a single-piece. Fig. 3-1(b) shows the top view of the diplexer where the asymmetric filter coupling elements are observed. The asymmetric irises are manufactured on the central common wall, preserving continuity of the high currents located in proximity of the irises (refer to Fig. 3-2). Two flat metal plates (not shown in figure) close the structure on the sides, providing optimum metal-to-metal contact at lower current regions.

Compared to conventional diplexer designs, the following advantages in terms of electrical performance are envisaged:

- higher Q factor;
- lower risk of RF emission;
- lower susceptibility to PIM generation.

Additional benefits associated to this layout are:

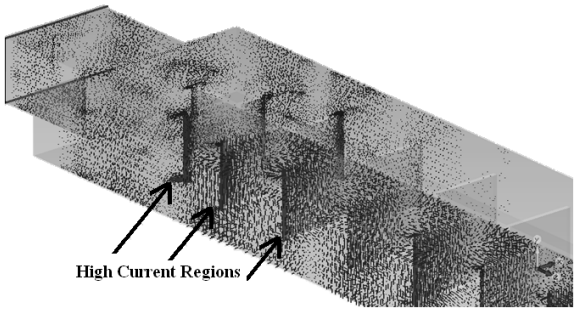

Fig. 3-2: High current areas, FEM simulation with CST MW Studio.

- simplified assembly process (no need of dowel pins, alignment jigs and special instructions for the operator);
- improved robustness to manufacturing tolerances (only one deviation from nominal size for each iris);
- overall lower costs.

These considerations are general and independent of the operating frequency. However the described design advantages are appreciable in particular for Ka-Band and other millimeter-wave applications.

3.1.2 Diplexer specifications and network model

To verify the performance of this diplexer concept in a practical Ka-Band context, the following RF specification are considered:

Usable bands	
Transmit (Tx)	19.3 to 19.8 GHz
Receive (Rx)	18.3 to 18.8 GHz
Insertion loss over pass band	
Tx	-0.5 dB
Rx	-0.8 dB
Return loss over pass band	
Tx	-28 dB
Rx	-28 dB
Rejection	
of Tx channel at Rx band	-90 dB
of Rx channel at Tx band	-110 dB

EMC (RF emission) and PIM are other important requirements in many applications. Typical figures at Ka-Band are -70 dBi for RF emission and -120 dBm for 3rd order PIM product.

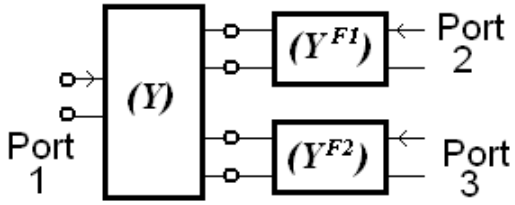

Fig. 3-3: Block diagram of the diplexer network.

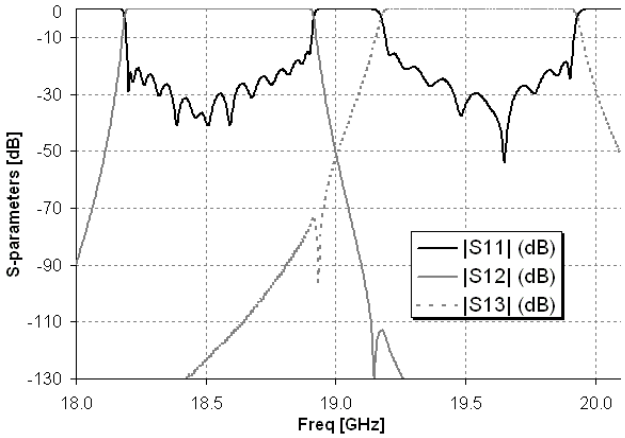

Fig. 3-4: Diplexer S-parameter network response.

A diplexer is a three port device that can be modelled using a 3x3 admittance or impedance matrix. Fig. 3-3 indicates the block diagram of the diplexer network model, where the junction is represented by the admittance matrix Y, and the two filters by the admittance matrices Y^{F1} and Y^{F2}. This model was used to calculate the diplexer S-parameter response and to determine the appropriate order of the filters using the equations given in [6]. The frequency bands were enlarged to include design margins (200 MHz for each band). It was calculated that 10 poles (Tx filter) and 14 poles (Rx filter) would be sufficient to achieve the specification as shown in Fig. 3-4. The diplexer response was calculated analytically, optimization of the return loss was not considered necessary at this level.

3.1.3 Dimensional synthesis and experimental results

The diplexer dimensions have been obtained using MM techniques. First, the stand-alone bifurcation was optimized for best match by adjusting the dimension D in Fig. 3-5. Based on the network analysis, the diplexer was designed applying the dimensional synthesis procedure described in [7] valid for non-contiguous pass bands. Such procedure provided an in band return loss of approximately -20 dB for both channel filters without any global optimizations. In order to achieve the stringent return loss specification, another optimization step was necessary. With respect to Figure 5, L0, L1, L2, R0, R1, R2, A1, A2, B1 and B2 were set as optimization variables. Target for the optimization was a return loss lower than -30 dB for both channel filters. The overall design time was considerably short, about 15 minutes on a standard PC.

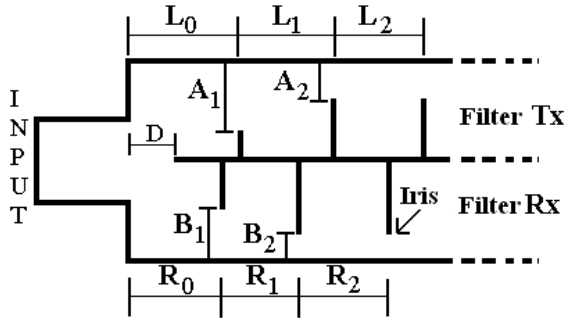

Fig. 3-5: Diplexer S-parameter network response.

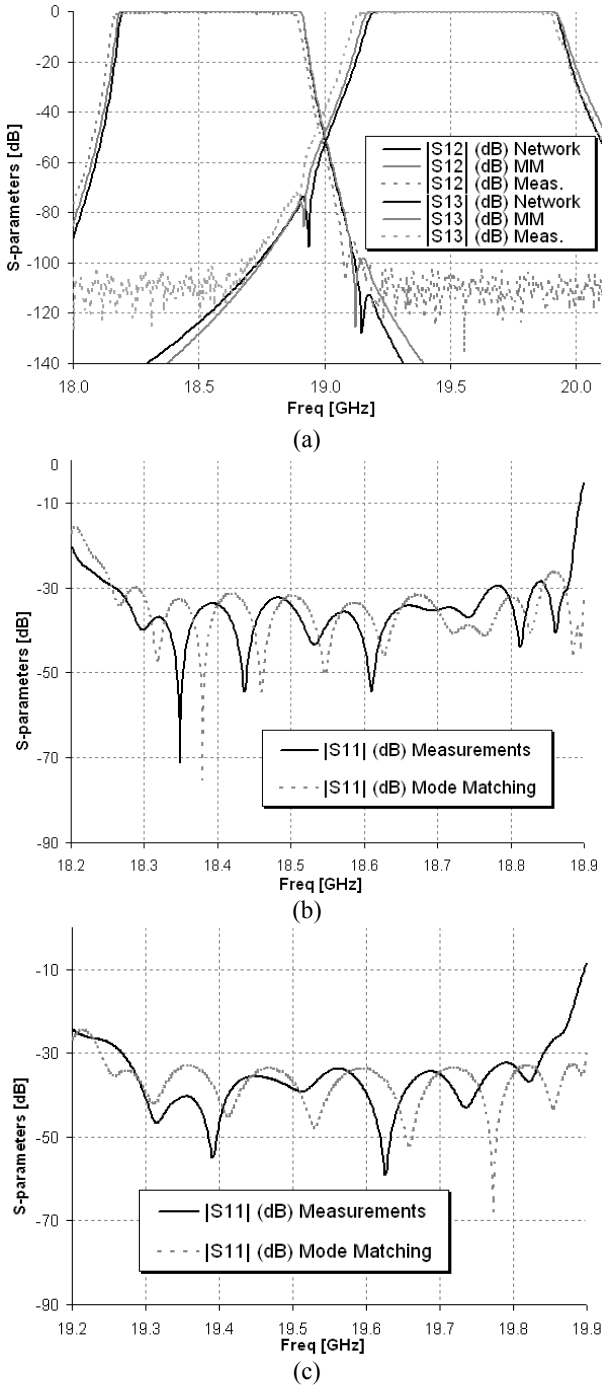

Fig. 3-6: Measurements against simulations. (a) Insertion Loss; (b) Rx Filter Return Loss; (c) Tx Filter Return Loss.

The engineered layout allowed simple manufacturing and assembling of a silver-plated aluminium prototype. In this case, spark machining was used; however lower cost techniques such as milling machining would also be possible in many broadband applications.

The prototype was tested at ambient conditions. Measured amplitude response is presented in Fig. 3-6(a) against simulations. Return loss results are provided in Figure 3-6(b) and Figure 3-6(c) versus simulated performance. Excellent agreement between the full-wave simulation and the experimental data is observed. All required RF specifications are met with adequate margin. In particular, return loss better than -30 dB is obtained over both specified pass bands, without tuning or post-production adjustments. These results are particularly impressive for Ka-band, considering

the small fractional bandwidths and the high filter orders. EMC and PIM performances have not been verified by test in this case, however very good performance is expected on the basis of the design considerations given in Sec. 3.1.1.

3.2 Composite corrugated filters with spurious rejection

Low-pass filters find extensive use in microwave and millimetre wave systems as important components rejecting unwanted spectrum over broad frequency ranges. Broad stop-band, low insertion loss, high power handling capability, minimum size and simple manufacturing are the key requirements in similar applications. Unfortunately, these features are in conflict when designing conventional filters and a trade-off has to be made. Ultimate consequence is the increasing difficulty to meet technical requirements of modern applications.

Three categories of waveguide low-pass filters have been studied by microwave engineers in the past: stepped-impedance (corrugated), waffle-iron and ridged filters.

Corrugated waveguide filters were firstly introduced by Cohn [8] in late 1940s. Later design methods using modern circuit theory and synthesis techniques have been developed by Levy [9] and generalized for wide class of tapered corrugated waveguide filters. The inconvenience of spurious pass-bands corresponding to high order modes was reported in [9], [10] and further investigated in [11]. The spurious pass-bands cannot be eliminated although their location can be predicted and eventually moved up or down the frequency axis by changing width of the corrugated waveguide. The spurious bands are due to the E-plane symmetry of structure, which is the baseline of this design. Since most of the energy propagates in the dominant mode, usually only narrow spurious components or "spikes" occur. While Hauth introduced an efficient analysis method [12] and described modifications to the corrugated filter in order to use it as a bandpass filter [13], Levy's work was later generalized to the inhomogeneous case [14]. Although latest Levy's approach improves the filter rejection performance, two separate points remain open: a) high-order spurious spikes are quite difficult to control (see [14, p. 124]) and are not acceptable in many applications; b) standard closed-form formulas are used, requiring major trade-offs between stop-band, insertion loss and power handling (see [9, p. 526]) and limiting the design flexibility. More recent studies on Bragg-reflector filters [15] did not address the spurious effects associated to modes of order higher than TE_{10} and a follow-up publication [16] shows solutions rather lossy, bulky and complex to manufacture.

Corrugated filters previously reported are based on waveguide structures susceptible to propagation of high order modes within the design stop-band. Modes of order higher than dominant are always present in any practical microwave systems due to discontinuities associated to both manufacturing inaccuracies (asymmetries, misalignments, etc.) and external mode exciters (transformers, bends, adapters, etc.). Since the filter out-of-band mode composition is in principle unknown, the worst-case excitation must be taken into account if rejection specifications are to be met without spurious.

Design methods employed in the conventional filter types are based on distributed or lumped element circuits. Target of those design methods is the synthesis of an equi-ripple filter response by pass-band and roll-off requirements. As a result, the in-band frequency response may well reproduce ideal polynomials such as Chebyshev or Zolotarev. In practice, those filters may not as well meet the rejection requirements. In the out-of-band frequency range, the original model used for in-band synthesis is no longer valid. Conventional design methods therefore ignore information about critical points corresponding to high-order modes, which form pass-bands or stop-bands. However the only effective method to design a spurious-free filter must be based on the proper

distribution of those critical points over the required out-of-band frequency range, in order to guarantee full coverage of reflection zeros by transmission zeros.

Waffle-iron filters [17], [18] are susceptible to generation of spurious spikes in the pass-band, roll-off and stop-band [18], [19]. These spikes are caused by excitation of waveguide modes not considered by established design methods. Limited power handling is another major disadvantage. Waffle-iron filters are therefore rarely employed in applications requiring both spurious-free and high power performance.

Evanescent-mode ridge waveguide filters [20], [21] require quite small gap sizes in order to provide sufficient out-of-band rejection in most of applications. Therefore quality factor and peak power handling capability of the ridged filter are significantly lower than non-evanescent type of filters. Tuning could also be required to compensate the high sensitivity to manufacturing tolerance. Ridged filters are therefore not suitable to those applications requiring very low losses or high power handling capability.

In addition to rejection performance, conventional synthesis techniques limit the low-pass filter designer to control other important features such as insertion loss, power handling, size and manufacturability, which are not directly associated to filter prototypes. On the other hand recent developments of computer technologies have made possible direct optimization of whole filter structures for specific requirements. For harmonic filters, optimization methods would allow to bypass the constrains of synthesis techniques, offering distinct advantages in terms of (multi-mode) rejection performance and design flexibility. An optimal *practical* filter could then look quite different from any classical prototype.

3.2.1 Cavity model and transmission zeros

The concept of direct-coupled cavities is the fundamental model describing reflection and transmission properties of a corrugated filter as non-uniform waveguide in multi-mode condition of propagation. In order to illustrate the basic properties of a single cavity element as building block of high-performance low-pass filters, a simple equivalent network is considered first. Fig. 3-7(a) shows the symmetric corrugation composed by a T-junction loaded by a shorted waveguide stub, whereas the equivalent network following a model from Marcuvitz [22] is derived in Fig. 3-7(b). The Π-network admittance parameters are calculated as:

$$\begin{cases} Y_{12} = -j \cdot \left(B_b + B_c \cdot \dfrac{B_d - \dfrac{b}{s}\cot(\beta h)}{B_d - B_c - \dfrac{b}{s}\cot(\beta h)} \right) \\ Y_{11} - Y_{12} = Y_{22} - Y_{12} = jB_a \end{cases} \tag{3.1}$$

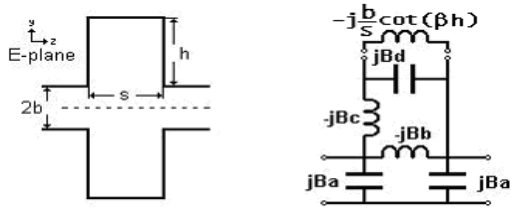

(a) (b)

Fig. 3-7: Symmetric E-plane cavity. a) 2D view; b) Equivalent network.

where the admittance Y_{12} turns into zero for:

$$\beta h = (2n+1)\frac{\pi}{2} - a\tan\left(\frac{s}{b}\left(B_d - \frac{B_b B_b}{B_c + B_b}\right)\right), n = 0,1... \tag{3.2}$$

The reflection and transmission coefficients of the single cavity can be expressed in elementary functions as follows:

$$\begin{cases} R(f) = \dfrac{1 - Y_{in}}{1 + Y_{in}} \\ T(f) = Y_{12} \cdot \dfrac{1 + R(f)}{1 + jB_a + Y_{12}} \end{cases} \tag{3.3}$$

in which

$$Y_{in} = jB_a + \frac{Y_{12}(1 + jB_a)}{1 + jB_a + Y_{12}} \tag{3.4}$$

Simple inspection of (3.1) shows that when Y_{12} turns into zero, the transmission coefficient T also inverts into zero. Each extracted cavity then forms transmission zeros (Fig. 3-8) located between frequency bands of moderate transmission. Therefore the cavity element can be used as low-pass unit or high-pass unit. In the vicinity of a given transmission zero f^{TZ}, we consider a bandwidth Δf where the transmission coefficient magnitude T shall be smaller than the corresponding specified value T_{min}. There is also a plurality of frequency points where the reflection coefficient R is approximately equal to zero. This happens at the cut-off of each mode and at the frequency points where Y_{12} is near infinity.

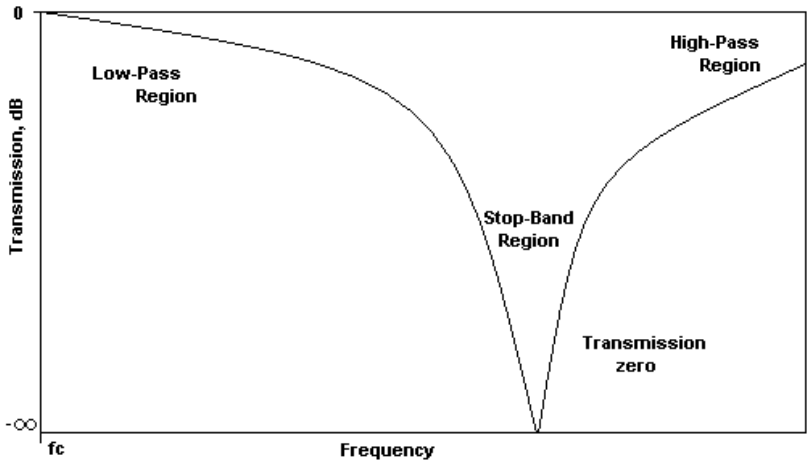

Fig. 3-8: Transmission response of a single cavity element.

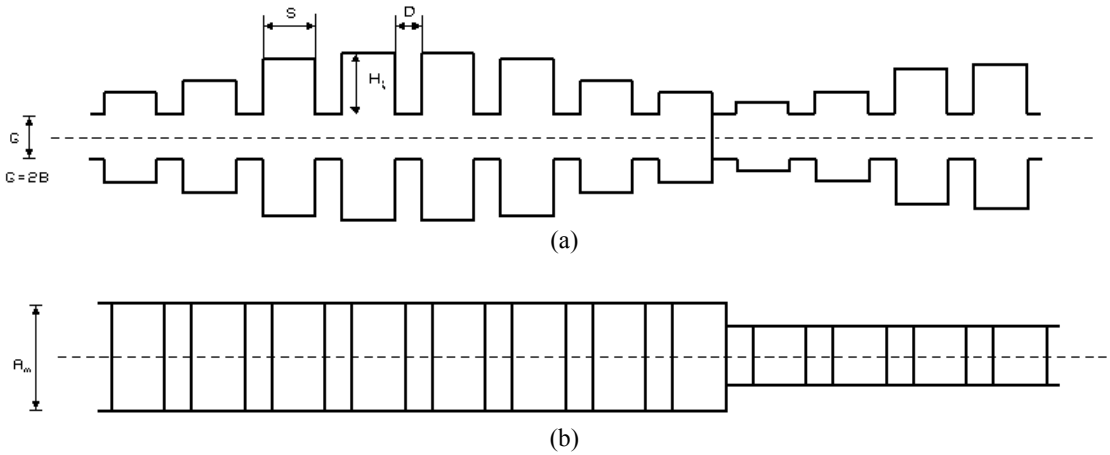

Fig. 3-9: Composite Corrugated Filter consisting of m partial filters. a) Side view; b) Top view.

3.2.2 Composite Corrugated Filters

Composite corrugated filters are generated via direct connection of m quasi-periodic E-plane tapered waveguides (partial filters), internally matched without intermediate transforming networks (Fig. 3-9). The composite structure is formed by $N = N_1+N_2+\ldots+ N_m$ cavities in series, with coupling gap g, length s and spacing d. The cavity length s is much shorter than $\lambda_g/10$. The cavity height h_i is gradually tapered from $h_{\min}$ at the ends to $h_{\max}$ at the center of each partial filter.

Although the structure of Fig. 3-9 physically resemble Levy's inhomogeneous filter, there is a substantial difference from the electrical viewpoint. The filter considered is based on short extracted cavities, realizing N transmission zeros in the stop-band (only first root n=0 for each cavity is used). The order N is *not* associated to the number of in-band reflection zeros and cannot be unambiguously associated with performance required. Therefore N is a secondary parameter and can be initially set to a value of 20±2 (for third harmonic rejection). This approach differs from classic corrugated filter theory where an N-pole TE_{10} mode response is synthesized using a capacitive iris or stepped-impedance transmission line model [9].

Assuming a gap g relatively smaller than the waveguide widths a_m, we can limit our consideration to only TE_{n0} modes in the analysis of the stop-band. An image frequency for the TE_{n0} mode of the m-th partial is predicted by (3.5), which is a generalized version of the formula of [9]:

$$f_{n,m} = \sqrt{f_m + 34.829\,\frac{n^2-1}{a_m^{\,2}}} \tag{3.5}$$

where f_m is a frequency point of the dominant mode and a_m is the waveguide width in inches of the m-th filter.

The multi-mode transmission responses can be represented as schematic graphs for the m filters to generate mode charts. Selecting partial filters with different widths, the pass-bands corresponding to spurious TE_{n0} modes can be positioned relatively to each other in such a way that no mutual frequency points exist. In this case any of the TE_{n0} modes carrying spurious frequency spectrum in one of the partial filters will be rejected by the other partial filter. This condition is called "strong", since it provides rejection of spurious frequency spectrum carried by all modes except the dominant one. When the position of spurious pass-bands corresponding to both partial filters intersects each other and the intersecting modes have different symmetry indexes, the condition is called "weak". Weak condition also guarantees that no spurious mode can propagate through the overall filter provided that ideal symmetry is maintained. Both conditions of spectrum superposition can be

adopted for design using (3.5). However it shall be mentioned that the weak condition provides in practice less rejection due to conversion between symmetric and asymmetric modes when asymmetries are introduced by manufacturing inaccuracies.

The criterion used to select the g dimension (expressed in inches) is based on imposing the cross-polarized TE_{01} waveguide mode to not propagate through the filter, i.e.:

$$g \le 0.5 \cdot \frac{f_c}{f_{sp,\max}} \tag{3.6}$$

where f_c is the dominant mode cut-off frequency of the lowest partial filter, $f_{sp,\max}$ is the highest frequency point of the specified stop-band and 0.5 is an empirical coefficient to account for the cavity loading effect.

The lengths s define the cavities Q-factor at the transmission zeros and are optimally selected using the empirical formula:

$$1.2 \cdot g \le s \le 1.4 \cdot g \tag{3.7}$$

where increasing the s value enlarges the transmission zeros bandwidth Δf, at the price of stronger spurious effects of higher order resonances.

The spacing between cavities d is set to the minimum value technologically feasible. Small values of d widen the overall stop-band, reducing at the same time the filter loss and length. In addition, a minimum value of d maximizes the g/d ratio, exploiting fringing-field effects to further increase the peak power handling capability in vacuum [23].

For each partial filter, the minimum cavity depth $h_{\min}$ depends on the highest specified frequency point of stop band $f_{sp,\max}$, where rejection is required. The maximum value for $h_{\min}$ – related to the first root of $Y_{12}(f_{sp,\max})$ when h is a variable – can be approximately evaluated as the stub length at resonance frequency, including an empirical loading factor:

$$h_{\min} \le 0.9 \cdot \frac{\pi}{2 \cdot \beta(f_{sp,\max})} \approx \frac{3.0}{f_{sp,\max}} \tag{3.8}$$

The ideal composite corrugated filter presents optimal distribution of transmission zeros formed by each cavity so that any frequency point of the design stop-band is within the rejection bandwidth Δf of at least one cavity. At the same time, the tapering function has to be adequately smooth in order to minimize the change of the scattering properties along the structure. A good compromise is found choosing the sine distribution as tapering function:

$$h_i = h_{\min} \cdot \left(1 + \varepsilon \cdot \sin^{\gamma}\left(\pi \cdot i / N_m\right)\right) \tag{3.9}$$

where $\varepsilon = (h_{\max} - h_{\min})/h_{\min}$.

The parameter ε is linked to the filter roll-off and γ defines the transmission zeros distribution from the roll-off, i.e., the transmission zeros cluster moves up in frequency when increasing γ. The smaller γ-values (between 1.0 and 1.5) lead to sharp but narrow-band rejection, which is recommended for rejecting up to the second harmonic. The larger γ-values (between 1.5 and 3.0) lead to a smooth but wide-band rejection and are better for third harmonic rejection. Imposing the γ value, the parameter ε is determined as a root of equation:

$$\left|T_{partial}\left(f_m, \vec{h}(\varepsilon)\right)\right| - T_{\min} = 0 \tag{3.10}$$

where, for a given partial filter

$T_{partial}(f,\vec{h}) = \left|S_{21}^{cascade}(f,\vec{h})\right|$ dominant mode transmission coefficient

$\vec{h} = (h_1,..., h_{N-1}, h_N)$ vector of cavity heights

f_m characteristic frequency where the filter dominant mode transmission coefficient equals $T_{\min}$.

The non-linear equation system of (3.8) and (3.9) can be easily solved with numerical methods.

The use of extracted cavities with sinusoidal distribution could result in non-ideal pass-band return loss and near-band rejection, because reflection zeros can appear around the roll-off range. But *for low-pass filters*, this is irrelevant when compliance to specifications is considered: pass-band return loss can be easily optimized (if required) as the initial structure is already internally matched; near-band performance is not a low-pass design driver as its function is to provide far-band and harmonic rejection.

3.2.3 Optimization tools and design procedure

Mode chart is the analytical tool from equation (3.5), used to perform preliminary spectrum superposition and determine the optimum waveguide widths a_m and roll-off frequencies of each m-th filter.

The *fast multi-mode simulator* is a code which loads the schematic file with the filter design dimensions and outputs frequency response data. The code model is based on a variational formulation that takes both fundamental and higher order modes into account. Fig. 3-10(a) depicts a cavity of length L formed by two step-junction discontinuities, in the general case of asymmetric rectangular-to-rectangular waveguide discontinuities with different accessible modes. A rigorous formulation in terms of Y- and B-matrices is presented in [24], which can be used for computing of the multimodal S-parameters of generic uniaxial waveguide discontinuities. Although with such an approach the cavity element of Fig. 3-10(a) can be characterized by cascade of S-matrices of two step-junctions, using an independent model for the double discontinuity gives the advantage of a more efficient computational algorithm. The expressions of the Y-matrix members are expressed as:

$$\begin{cases} Y_{ks}^{11} = \sum_n y_n \dfrac{\alpha_{kn}^{(1)}\alpha_{sn}^{(1)}}{j\tan(\beta_n L)} & Y_{ks}^{12} = -\sum_n y_n \dfrac{\alpha_{kn}^{(1)}\alpha_{sn}^{(2)}}{j\sin(\beta_n L)} \\ Y_{ks}^{21} = -\sum_n y_n \dfrac{\alpha_{kn}^{(2)}\alpha_{sn}^{(1)}}{j\sin(\beta_n L)} & Y_{ks}^{22} = \sum_n y_n \dfrac{\alpha_{kn}^{(2)}\alpha_{sn}^{(2)}}{j\tan(\beta_n L)} \end{cases} \tag{3.11}$$

where the α-values are the aperture integrals on both accessible ports *g1* and *g2*:

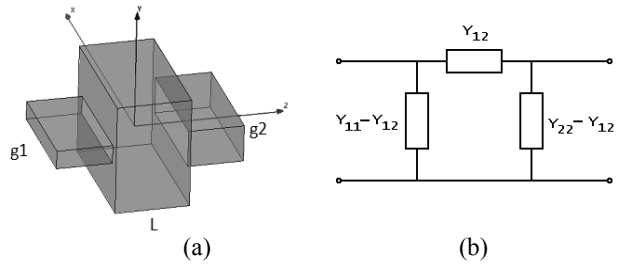

(a) (b)

Fig. 3-10: Single waveguide cavity. a) 3D view; b) Equivalent network.

$$\alpha_{kn}^{(1)} = \iint_{g1} \underline{E}_k^{(1)} \cdot \underline{E}_n dxdy \qquad \alpha_{sn}^{(1)} = \iint_{g1} \underline{E}_s^{(1)} \cdot \underline{E}_n dxdy$$

$$\alpha_{kn}^{(2)} = \iint_{g2} \underline{E}_k^{(2)} \cdot \underline{E}_n dxdy \qquad \alpha_{sn}^{(2)} = \iint_{g2} \underline{E}_s^{(2)} \cdot \underline{E}_n dxdy$$

This rigorous model is used for fast and accurate modeling of a generally non-uniform corrugated waveguide using sequential cascading of multi-modal S-matrices. The process of simulation takes about two seconds on a standard PC for a typical filter structure with 20 corrugations, using one accessible mode and about 200 localized modes swept over 600 discrete frequency points.

The analytical formulation was initially reported in [25] but is formally derived here. With reference to Fig. 3-10, transverse electric and magnetic fields of a smaller waveguide on junction areas *g1* or *g2* can be represented in terms of Harrington's voltage and current factors [24] as follows:

$$\underline{E}_t^{(1,2)} = \sum_k v_k^{(1,2)}(z)\underline{E}_k^{(1,2)}(x,y) \tag{3.12}$$

$$\underline{H}_t^{(1,2)} \times z_0 = \sum_k i_k^{(1,2)}(z)\underline{E}_k^{(1,2)}(x,y) \tag{3.13}$$

where $v_k(z)$ and $i_k(z)$ correspond respectively to the sum and difference of incident and reflected wave amplitudes of the k-th mode at the accessible waveguides 1 and 2. $E_k(x,y)$ is the cross-section electric field of the k-th mode in the smaller waveguide normalized on *g1* or *g2*.

Electric and magnetic fields in the larger waveguide cavity are expressed as superposition of standing waves:

$$\underline{E}^{cav} = \sum_n \left\{A_n^1 \sin(\beta_n z) + A_n^2 \sin(\beta_n (L-z))\right\}\underline{E}_n \tag{3.14}$$

$$\underline{H}^{cav} \times z_0 = \sum_n jy_n \left\{A_n^1 \cos(\beta_n z) - A_n^2 \cos(\beta_n (L-z))\right\}\underline{E}_n \tag{3.15}$$

where A_n represents the modal amplitude of the n-th standing wave shorted at z = 0 and z = L respectively.

Projecting on eigen function basis E_n the boundary conditions for electric fields at the junction planes (G is the wall area of the larger waveguide at the junction):

$$\underline{E}^{cav}(x,y,0) = \begin{cases} \underline{E}^1(x,y,0) \text{ for } x,y \in g_1 \\ 0 \text{ for } x,y \in G - g_1 \end{cases} \tag{3.16}$$

$$\underline{E}^{cav}(x,y,L) = \begin{cases} \underline{E}^2(x,y,L) \text{ for } x,y \in g_2 \\ 0 \text{ for } x,y \in G - g_2 \end{cases} \tag{3.17}$$

we obtain

$$A_n^{(2,1)} \sin\left(\beta_n L\right) = \sum_n v_k^{(1,2)} \alpha_{k,n}^{(1,2)} \tag{3.18}$$

and substituting

$$\widetilde{A}_n^{(2,1)} = A_n^{(2,1)} \sin\left(\beta_n L\right) \tag{3.19}$$

then

$$\widetilde{A}_n^{(2,1)} = \sum_k v_k^{(1,2)} \alpha_{k,n}^{(1,2)} \tag{3.20}$$

Projecting on eigen function basis $\underline{E}_k^{(1,2)}$ the continuity conditions of magnetic field at apertures:

$$\underline{H}^{cav}(x, y, 0) \times z_0 = \underline{H}_t^{\,1}(x, y, 0) \times z_0 \quad \text{for } x, y \in g_1 \tag{3.21}$$

$$\underline{H}^{cav}(x, y, L) \times z_0 = \underline{H}_t^{\,2}(x, y, L) \times z_0 \quad \text{for } x, y \in g_2 \tag{3.22}$$

and manipulating the resulting equations, we obtain:

$$i_k^{(1,2)} = \pm \sum_n jy_n^{(1,2)} \left\{ \frac{\widetilde{A}_n^{(1,2)}}{\sin(\beta_n L)} - \frac{\widetilde{A}_n^{(2,1)}}{\tan(\beta_n L)} \right\} \alpha_{kn}^{(1,2)} \tag{3.23}$$

where

$$\alpha_{kn}^{(1,2)} = \iint_{g1, g2} \underline{E}_k^{(1,2)}(x, y) \cdot \underline{E}_n(x, y) dxdy \tag{3.24}$$

Substituting (3.20) into (3.23) and introducing the index *s* for the *s*-th mode in the smaller waveguide, we obtain the expressions (3.11) of the Y-matrix.

The *transformer synthesizer* is a code based on conventional matching techniques, which loads simulation file with initial specification and generates a partial filter matched around the central frequency of pass-band via step transformer. Such techniques are widely known and therefore not repeated here. The program outputs schematic file with design dimensions. Time of the synthesis process takes less than one second on a standard PC, when applied to typical filters with 20 corrugations.

For design optimization an error function to be minimized is constructed with the cavity spacing *d* and transformer lengths as optimization variables. Only waveguide lengths are used to tune the filter response, thus the procedure is very fast since only a step characterization is required all over the optimization process. Time of the optimization process normally takes less than 10 minutes on a standard PC when applied to typical filters with 20 corrugations. This step can be often omitted, particularly in all cases where standard return loss level (around -20 dB) are required.

The design procedure is summarized in the following steps.

Step 1) Filter widths and roll-off frequencies are selected using the mode chart generated from (3.5).
Step 2) With the aid of the multi-mode simulator, initial parameters of each partial filter are determined using the design formulas (3.6), (3.7), (3.8), (3.9) and (3.10).
Step 3) The partial filters are first matched individually using the transformer synthesizer and then directly connected into a composite filter.
Step 4) With the aid of the multi-mode simulator, check that specified stop-band is clear from TE_{n0} spurious spikes.
Step 5) (If required) Fine-tune the pass-band return loss and verify performance.

The procedure requires running many simulations of different waveguide modes for several design iterations. Any modal analysis technique can be in principle employed, being the procedure completely general. However, it is found that the approach becomes particularly fast using the multi-mode variational formulation discussed above, since most of complex matrix manipulations are replaced by two-dimensional sums. Overall design process is then a matter of few minutes, including optimization.

The fundamental difference of this method with respect to synthesis emerges now in its full extent. Here the multi-mode stop-band performance is determined *before* the pass-band implementation, imposing the largest g and the smallest d values, then tapering the corrugation heights. The advantages resulting from this approach are the broad rejection free of spurious TE_{n0} bands and the optimal dimensional features. Previous methods proceed somewhat backwards: an equi-ripple pass-band is synthesized as a first step, loosing information about spurious modes and leading to small-gap and lengthy structures associated to filter prototypes.

Similarly to [14], bandwidth limitation is the disadvantage of using composite filters. The maximum bandwidth is limited by the TE_{10} mode cut-off frequency of the waveguide of smallest width and the lowest roll-off frequency (actual limitation can be easily estimated with the mode-chart). Using this approach fractional bandwidths up to 20% are typically achieved. These encompass the majority of applications.

3.2.4 Example: Ku-Band output filter

In the frame of a recent Ku-Band space flight program, a low-pass filter in WR-75 waveguide was required after high-power amplification in a remote location of the spacecraft. The filter must provide broad rejection free of spurious TE_{n0} bands, according to the following specifications:

Pass band	11.2 to 12.5 GHz
Insertion loss over pass band	-0.12 dB
Return loss over pass band	-26 dB
Rejection	
from 17.3 to 18.1 GHz	-80 dB (K-Band Rx)
from 22.4 to 18.1 GHz	-60 dB (2^{nd} harmonic)
from 33.6 to 37.5 GHz	-60 dB (3^{rd} harmonic)
Power handling (multipactor)	6205 W
Length	6 in

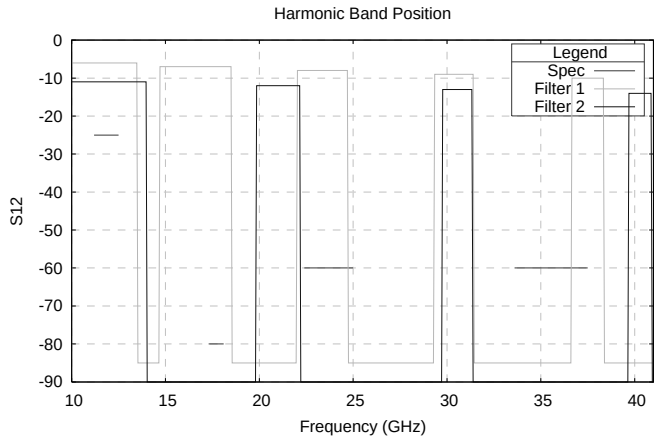

Fig. 3-11: Mode chart for the first four TE_{n0} modes: TE_{10}, TE_{20}, TE_{30} and TE_{40}.

Note: good performance over a broader frequency range would be desirable as a design target. Specifically, the filter should feature a pass-band between 10.7 and 12.7 GHz with return losses below -26 dB. Moreover, a clean rejection level should be maintained for frequencies between 17.3 GHz and 40.0 GHz. Although not formal requirements, these targets would lead to a more generic design suitable to a variety of Ku-Band high-power applications.

Fig. 3-11 shows the mode chart, where both strong and weak conditions are used for spurious suppression ($a_1 = 0.805$ in, $a_2 = 0.595$ in).

Using eq. (3.6) and (3.7) at the highest specified frequency point $f_{sp,\max} = 37.5$ GHz and imposing d, the first set of design dimensions was determined ($g = 0.08$ in, $d = 0.05$ in, $s = 0.09$ in). The minimum cavity height was calculated from (3.8) ($h_{\min} = 0.08$ in). Setting the order of the two partial filters ($N_1 = 10$, $N_2 = 8$), then selecting γ ($\gamma_1 = 2$, $\gamma_2 = 3$) and solving the two resulting non-linear equation systems (for both cases: $\varepsilon \approx 1.75$, $h_{\max} = 0.22$ in), the other elements of the heights vector are calculated. The two partial filters are matched to WR75 via 2-step transformers at one end, then connected together without any transformer at the other end.

It can be noted how eq. (3.6), (3.7), (3.8), (3.9) and (3.10) provide very good initial values, so that the fast multi-mode simulator is only used for minor adjustments of g, γ_1, γ_2 while monitoring the spurious performance (Fig. 3-12).

The pass-band performance of Fig. 3-12(a) shows good matching without any full-wave global optimization. In order to meet the stringent return loss requirement, minor optimization of the cavity spacing d and transformer lengths was necessary in this example. Final lengths are within ±0.010 in of the starting values.

The final RF performance, including insertion loss and peak voltages, was verified via commercial numerical tools (CST Microwave Studio). Fig. 3-13 depicts a 3D view of the final structure half-shell ready for manufacturing.

The *filter response* in Fig. 3-12(a) may look non-optimal in terms of polynomial prototypes: there is no correspondence between number of poles and number of cavities and one reflection appears in the roll-off range around 15 GHz. But the *filter structure* looks really optimal at the eyes of an experienced filter designer: the large gap size g shows promise of high power handling, low loss and low sensitivity to mechanical tolerance; the short cavities and simple matching networks results in a compact size (length is less than 6 in); the filter body is straightforward from the manufacturing viewpoint and can be realized using conventional clam-shell techniques.

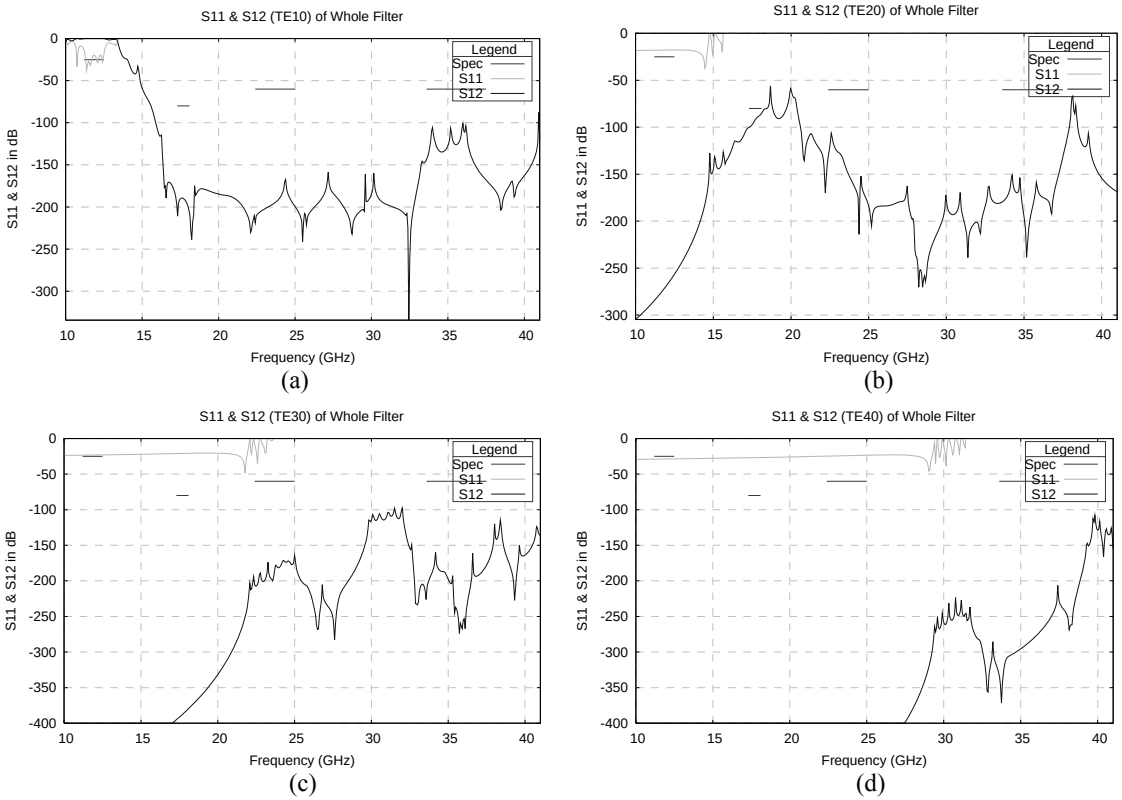

Fig. 3-12: Multi-mode simulator response of the first four TE_{n0} modes: TE_{10}(a), TE_{20}(b), TE_{30}(c) and TE_{40}(d).

.

The filter was built from two aluminum body halves using industry standard machining process, silver-plated and fastened by mounting screws.

Fig. 3-13 show the low-power S-parameters measured results, without any tuning. The in-band performance shows a return loss better than -28 dB and an insertion loss around -0.10 dB. The out-of-band measurement of Fig. 3-14 was carried out over frequency range from 13.0 to 40.0 GHz divided into three sub-bands, i.e.: 13.0 to 20.0 GHz, 20.0 to 30.0 GHz and 30.0 to 40.0 GHz. The filter WR75 waveguide interface is connected to the dominant mode waveguide corresponding to each sub-band through waveguide tapers, ensuring the measured signal is converted into the TE_{10} mode. In order to achieve worst-case excitation of both symmetric and asymmetric modes within the specified stop-band, special mode exciters (H-plane bends) are placed at the filter input and output ports [11]. The resulting multi-mode standing wave between tapers is reduced by attenuating sections installed before the exciters and calibrated out. As can be seen in Fig. 3-14, the out-of-band

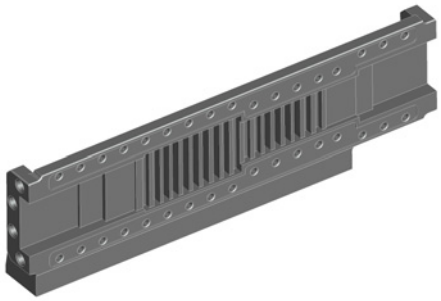

Fig. 3-13: ProE view of the fabricated filter (only one half-shell shown).

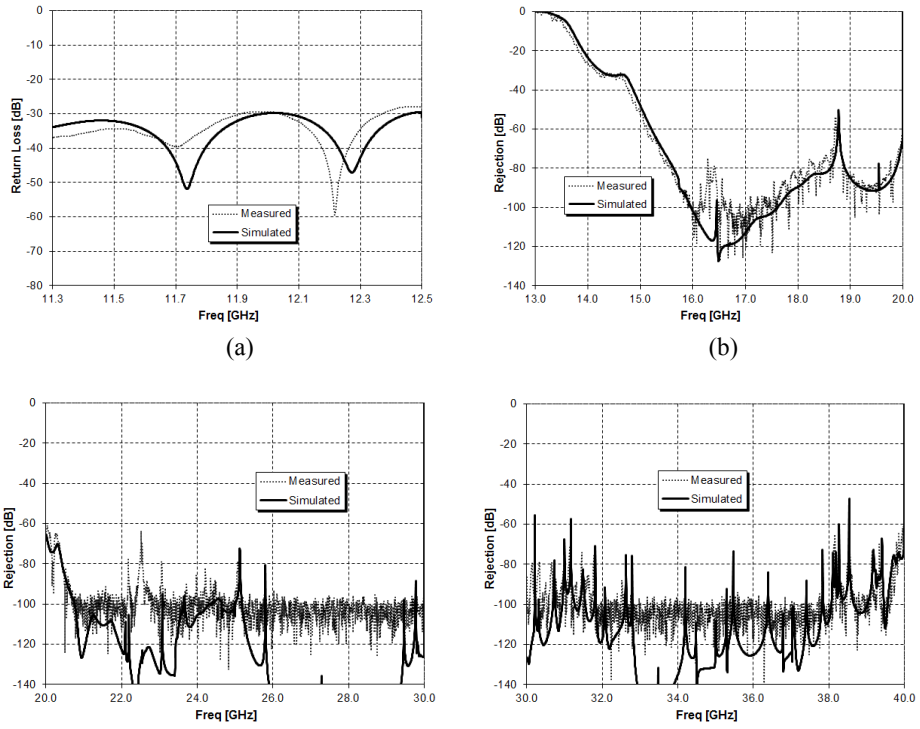

Fig. 3-14: Measured performance over several frequency ranges. (a) In Band Return Loss. (b) Rejection from 13.0 to 20.0 GHz. (c) Rejection from 20.0 to 30.0 GHz. (d) Rejection from 30.0 to 40.0 GHz.

range is free of spurious TE_{n0} bands beyond the third harmonic. Only minor narrow-band spikes are observed. Such spikes are mainly due to the TE_{20} mode, as expected via simulation of Fig. 3-12(b). It is important to remark that a "clean" out-of-band rejection – similarly to the plots of Fig. 3-12(a) – is obtained when the filter is used in a symmetric waveguide system, where high order modes are considerably lower [11].

The filter was high-power tested for multipactor breakdown. The setup consisted of an RF pulsed source (power level = 6205 W, test frequency = 11.717 GHz, duty cycle = 2%), a thermal-vacuum chamber (control temperature = 82 °C, pressure < $5 \cdot 10^{-5}$ torr) and a Cesium radioactive source for electron seeding. Close-to-carrier noise, 3rd harmonic and e-probe were used as detection methods. No multipactor events occurred up to the maximum power level required.

TABLE 3-1
KU-BAND FILTER PERFORMANCE SUMMARY

Unit	Parameter	Specification	Predicted	Measured	Notes
GHz	Usable Bandwidth	11.2 – 12.5	11.2 – 12.5	11.2 – 12.5	
dB	Insertion Loss	-0.12	-0.10 [a]	-0.10	Simulated with CST MWS
dB	Return Loss	-26	-30	-28	
dB	Rejection				
	17.3 to 18.1 GHz	-80	-85	-81	
	18.1 to 22.4 GHz	0	-55	-55	
	22.4 to 25.0 GHz	-60	-65	-63	
	25.0 to 26.0 GHz	0	-75	-78	
	26.0 to 33.6 GHz	0	-60	-77	
	33.6 to 37.5 GHz	-60	-75	-96	
	37.5 to 40.0 GHz	0	-50	-57	
W	Peak Power Handling	6205	>10000	6205 [b]	No Multipactor event detected
in	Length	6	5.9	5.9	

Table 3-1 summarizes the predicted and measured filter performance versus the technical requirements. It was possible not only to meet the stringent specifications, but also to provide good rejection (between -55 to -80 dB approximately) over a much broader range than required. Similar rejection levels cannot be guaranteed by conventional corrugated filters and are normally achievable only using waffle-iron or ridged filters, at the price however of reduced power handling, higher loss and/or increased manufacturing complexity. Using previously published design methods, it is not possible to simultaneously fulfill similar sets of requirements.

3.3 Summary

Novel design concepts are introduced in this chapter in order to improve the performance of high-power broadband filters.

A diplexer design concept is presented with an engineered layout which provides advantages from computational, electrical and manufacturing viewpoints. The design combines asymmetric inductive iris channel filters and a monolithic bifurcation. Network and full-wave methods are employed to efficiently model the diplexer, taking advantage of the H-plane symmetry of the overall structure. Compared to conventional waveguide diplexers, there are benefits associated to this approach in terms of electrical performance: higher Q factor, lower risk of RF emission, lower susceptibility to PIM generation. Additional advantages are the simple assembly process, robustness to manufacturing tolerances, and overall low costs. The design was validated by manufacturing and testing an 18/19 GHz prototype. The full-wave and measured return losses are in good agreement and below -30 dB over the specified pass bands. The results presented make this design concept attractive for both high performance and low cost applications at Ka-band and other millimeter-wave frequencies.

Computer-aided design based on multi-mode variational techniques takes minutes and leads to optimal solutions meeting modern requirements for waveguide low-pass filters. It is shown that composite corrugated structures can be utilized to form a multi-mode cluster of transmission zeros through fast design and optimization of the cavity heights. The designer has then full control over key dimensional features (gap g, length s and spacing d), that can be optimally pre-selected at the beginning of the design process. The following improvements are introduced with respect to previous techniques: 1) Rejection of harmonic spurious bands. It is possible to effectively design low-pass filters with spurious rejection for both fundamental and higher-order modes, irrespective of the excitation conditions of the system. 2) Enhanced design flexibility: it is possible to design low-pass filters with large gap size and short lines, without jeopardizing the harmonic spurious performance. This leads to a number of distinct benefits in parallel: low insertion loss, high power handling capability, small length and simple industrialization (no tuning, low sensitivity to mechanical tolerance, standard manufacturing process). Simulation and measurement results of a Ku-Band example demonstrated the feasibility of the method, in particular when rejection specifications up to the third harmonic are to be met without spurious. In many practical cases, out-of-band rejection, insertion loss, power handling capability, size and manufacturing complexity no longer need to be traded-off.

3.4 References

[1] J. Uher, J. Bornemann, U. Rosenberg, Waveguide Components for Antenna Feed Systems: Theory and CAD, Artech House, Boston – London, 1993.

[2] J. Dittloff, F. Arndt, "Rigourous field theory design of millimeter-wave E-plane integrated circuit multiplexers," IEEE Trans. Microwave Theory Tech., vol. 37, pp. 340-350, Feb. 1989.

[3] M.S. Uhm, J. Lee, D. Bae, I.B. Yom, S.P. Lee, "Ka band Waveguide Diplexer using E-plane T junction with inductive iris," APMC-2002, vol. 1, pp. 508-511, 2002.

[4] Y. Rong, H. W. Yao, K. A. Zaki, T. G. Dolan, "Millimeter-Wave Ka-Band H–Plane Diplexers and Multiplexers," IEEE Trans. Microwave Theory Tech., vol. 47, pp. 2325-2330, Dec. 1999.

[5] T. Shen, K.A. Zaki, T.G. Dolan, "Rectangular waveguide diplexers with a circular waveguide common port," IEEE Trans. Microwave Theory Tech., vol. 51, pp. 578-582, Feb. 2003.

[6] F.M. Vanin, F. Frezza, D. Schmitt, "Computer-aided design of waveguide Y-junction diplexers," PIER C Progress In Electromagnetics Research C, vol. 17, pp. 219-227, 2010.

[7] F.M. Vanin, D. Schmitt, R. Levy, "Dimensional synthesis of wideband waveguide filters and diplexers," in IEEE Trans. Microwave Theory and Tech., vol. 52, No. 11, pp. 2488-2495, Nov 2004.

[8] S.B. Cohn, "A theoretical and experimental study of a waveguide filter structure", Office Naval Res., Cruft Lab., Harvard Univ., Cambridge, Mass., Rep. 39, Apr. 25, 1948.

[9] R. Levy, "Tapered Corrugated Waveguide Low-Pass Filter", IEEE Trans. Microwave Theory Tech., MTT-21, August 1973, pp. 526-532.

[10] C.G. Matthaei, L. Young, and E. M. T. Jones, Microwave Filters, Impedance Matching Networks, and Coupling Structures, New York, McGraw-Hill, 1964.

[11] K. L. Wu and G. McDonald, "Coping with hidden spurious harmonic modes in design of low-pass corrugated waveguide filters," Microwave Journal, November 2001.

[12] W. Hauth, R. Keller, U. Rosenberg, "CAD of Waveguide Low-Pass Filters for Satellite Applications," 17th European Microwave Conference, Rome 1987, pp. 151 – 156.

[13] W. Hauth, R. Keller, U. Rosenberg, "The Corrugated Band-Pass Filter – A New Type of Waveguide Filter," 18th European Microwave Conference, Stockholm 1988, pp. 945 – 949.

[14] R. Levy, "Inhomogeneous Stepped-Impedance Corrugated Waveguide Low-Pass Filters," IEEE MTT Int. Micr. Symp. Digest., June 2006.

[15] I. Arregui, I. Arnedo, A. Lujambio, M. Chudzik, D. Benito, R. Jost, F. -J. Görtz, T. Lopetegi, and M. A. G. Laso, "A Compact Design of High-Power Spurious Free Low-Pass Waveguide

Filters," IEEE Microwave and Wireless Components Letters, vol. 20, no. 11, pp. 595-597, November 2010.

[16] I. Arregui, F. Teberio, I. Arnedo, A. Lujambio, M. Chudzik, D. Benito, R. Jost, F. -J. Görtz, T. Lopetegi, and M. A. G. Laso, "High-Power Low-Pass Harmonic Waveguide Filter With TEn0-Mode Suppression," IEEE Microwave and Wireless Components Letters, vol. 22, no. 7, pp. 339-341, July 2012.

[17] S. B. Cohn, E. M. T. Jones, J. K. Shimizu, B. M. Schiffman, and F. S. Coale, "Research on design criteria for microwave filters," Final report, Project 1331, Contract DA 36-039 SC-64625, Stanford Research Institute, June 1957.

[18] E. D. Sharp, "A High-Power Wide-Band Waffle-Iron Filter," IEEE Trans. Microwave Theory and Tech., March, 1963, pp. 111-119.

[19] L. Young and B. M. Schiffman, "New and improved types of waffle-iron filters," Proc. IEE (London), Vol. 110, JuIy 1963.

[20] H. F. Chappelle, "Waveguide Low Pass Filters Using Evanescent Mode Inductors", Microwave Journal, Vol. 2A, No. 12, December 1978, pp. 71-72.

[21] A. M. Saad, "Novel lowpass harmonic filters for satellite applications," IEEE MTT-S Int. Microwave Symp. Dig., May 1984, pp. 292-294.

[22] N. Marcuvitz, Waveguide Handbook. Piscataway, NJ, The Institution of Electrical Engineers, 1986.

[23] R. Udiljak, D. Anderson, M. Lisak, J. Puech, and V. E. Semenov, "Multipactor in a waveguide iris," IEEE Trans. Plasma Sci., vol. 35, No. 2, pp. 388-395, 2007.

[24] J.W. Tao and H. Baudrand, "Multimodal Variational Analysis of Uniaxial Waveguide Discontinuity," IEEE Trans. Microwave Theory and Tech., v. 39, No.3, March, 1991.

[25] R. Goulouev (RLC Electronics), "Basic Theory of Composite Filters," Microwave Product Digest, February 2007.

Chapter 4. Publications

International Journals

[1] F. De Paolis and F. Frezza, "Simplified Prediction of Peak Power Handling Capability for Stepped-Impedance Low-pass Filters", IEEE Trans. Microwave. Theory & Tech., vol. 61, no. 3, pp. 1079-1085, March 2013.

[2] F. De Paolis, R. Goulouev, J. Zheng and M. Yu, "CAD Procedure for High-Performance Composite Corrugated Filters", submitted to IEEE Trans. Microwave Theory and Tech., February 2013.

Conference Proceedings

[3] F. De Paolis, "Power Handling Prediction for Waveguide Harmonic Filters with Complex Geometry", submitted to APMC-2013, April 2013

[4] L. Pelliccia, F. Cacciamani, R. Sorrentino and F. De Paolis, "Compact High-Performance Filters for Space Applications based on Dielectric Resonator Technology", ESA Microwave Technology and Techniques Workshop, Noordwijk, The Netherlands, May 2012.

[5] C. Ernst, P. Angeletti and F. De Paolis, "Needs for Bandwidth Reconfigurable Filter Network for Space Applications ", ESA Flexible Payload Workshop, Noordwijk, The Netherlands, April 2012.

[6] F. De Paolis, F. Vanin and F. Frezza, "High-Performance Ka-Band Waveguide Diplexer with Engineered Layout", Ka and Broadband Communications Conference, Palermo, Italy, October 2011.

[7] V. Tornielli, F. De Paolis and D. Petrolati, "Ridge Waveguide Filter Design and Application to Multibeam Satellites", Ka and Broadband Communications Conference, Palermo, Italy, October 2011.

[8] F. De Paolis and D. Lemus, "Multipactor Assessment of the new U.S. 17/24 GHz Broadcast Satellite Service", International Workshop on Multipactor, Corona and Passive Intermodulation in Space RF Hardware, Valencia, Spain, September 2011.

[9] N. Le Gallou, C. M. Espanya, S. Matinfair, C. Ernst and F. De Paolis, "Multipactor Threshold and Margins Using Realistic Modulated Signals", International Workshop on Multipactor, Corona and Passive Intermodulation in Space RF Hardware, Valencia, Spain, September 2011.

[10] W. D'Orazio, O. De Meyer, F. De Paolis, C. Ernst, C. Miquel Espana and D. Raboso, “Liquid Cooled 400 Watt Output Multiplexer for ESA Multicarrier Test Facility”, ESA Microwave Technology and Techniques Workshop, Noordwijk, The Netherlands, May 2010.

[11] N. Sidiropoulos, S. A. Kosmopoulos, F. De Paolis, C. Ernst and G. Codispoti, “Design and Prototyping of a Tuning-Less Q/V Band Diplexer on Board the AlphaSat TDP#5 Payload”, CNES/ESA International Workshop on Microwave Filters, Toulouse, France, November 2009.